



Generative adversarial networks in medical image segmentation: A review



Siyi Xun^a, Dengwang Li^{a,*}, Hui Zhu^b, Min Chen^c, Jianbo Wang^d, Jie Li^e, Meirong Chen^f, Bing Wu^g, Hua Zhang^h, Xiangfei Chaiⁱ, Zekun Jiang^a, Yan Zhang^a, Pu Huang^{a, **}

^a Shandong Key Laboratory of Medical Physics and Image Processing, Shandong Institute of Industrial Technology for Health Sciences and Precision Medicine, School of Physics and Electronics, Shandong Normal University, Jinan, Shandong, 250358, China

^b Department of Radiation Oncology, Shandong Cancer Hospital and Institute, Shandong First Medical University and Shandong Academy of Medical Sciences, Jinan, Shandong, China

^c The Second Hospital of Shandong University, Shandong University, The Department of Medicine, The Second Hospital of Shandong University, Jinan, China

^d Department of Radiation Oncology, Qilu Hospital, Cheeloo College of Medicine, Shandong University, Jinan, Shandong, 250012, China

^e Department of Infectious Disease, Shandong Provincial Hospital Affiliated to Shandong University, Cheeloo College of Medicine, Shandong University, Jinan, Shandong, China

^f Affiliated Hospital of Shandong University of Traditional Chinese Medicine, Jinan, Shandong, China

^g Laibo Biotechnology Co., Ltd., Jinan, Shandong, China

^h LinkingMed Technology Co., Ltd., Beijing, China

ⁱ Huiying Medical Technology (Beijing) Co., Ltd., Beijing, China

ARTICLE INFO

Keywords:

Generative adversarial networks
Medical image
Segmentation
Deep learning
Computer vision

ABSTRACT

Purpose: Since Generative Adversarial Network (GAN) was introduced into the field of deep learning in 2014, it has received extensive attention from academia and industry, and a lot of high-quality papers have been published. GAN effectively improves the accuracy of medical image segmentation because of its good generating ability and capability to capture data distribution. This paper introduces the origin, working principle, and extended variant of GAN, and it reviews the latest development of GAN-based medical image segmentation methods.

Method: To find the papers, we searched on Google Scholar and PubMed with the keywords like “segmentation”, “medical image”, and “GAN (or generative adversarial network)”. Also, additional searches were performed on Semantic Scholar, Springer, arXiv, and the top conferences in computer science with the above keywords related to GAN.

Results: We reviewed more than 120 GAN-based architectures for medical image segmentation that were published before September 2021. We categorized and summarized these papers according to the segmentation regions, imaging modality, and classification methods. Besides, we discussed the advantages, challenges, and future research directions of GAN in medical image segmentation.

Conclusions: We discussed in detail the recent papers on medical image segmentation using GAN. The application of GAN and its extended variants has effectively improved the accuracy of medical image segmentation. Obtaining the recognition of clinicians and patients and overcoming the instability, low repeatability, and uninterpretability of GAN will be an important research direction in the future.

1. Introduction

With the rapid development and popularization of medical imaging equipment, a huge amount of medical imaging information is produced every day in the world. Medical image processing is the first step in the analysis of medical images, which makes images more intuitive to

improve the diagnosis efficiency. As an important part of image processing, image segmentation is a difficult problem, that restricts the application of 3D reconstruction and other technologies. In recent years, with the revival of deep learning in the field of computer vision (Litjens et al. (2017)) [1], the application of deep learning in the field of medical imaging has increased dramatically, and image segmentation algorithms

* Corresponding author.

** Corresponding author.

E-mail addresses: dengwang@sdu.edu.cn (D. Li), pu.wong@139.com (P. Huang).

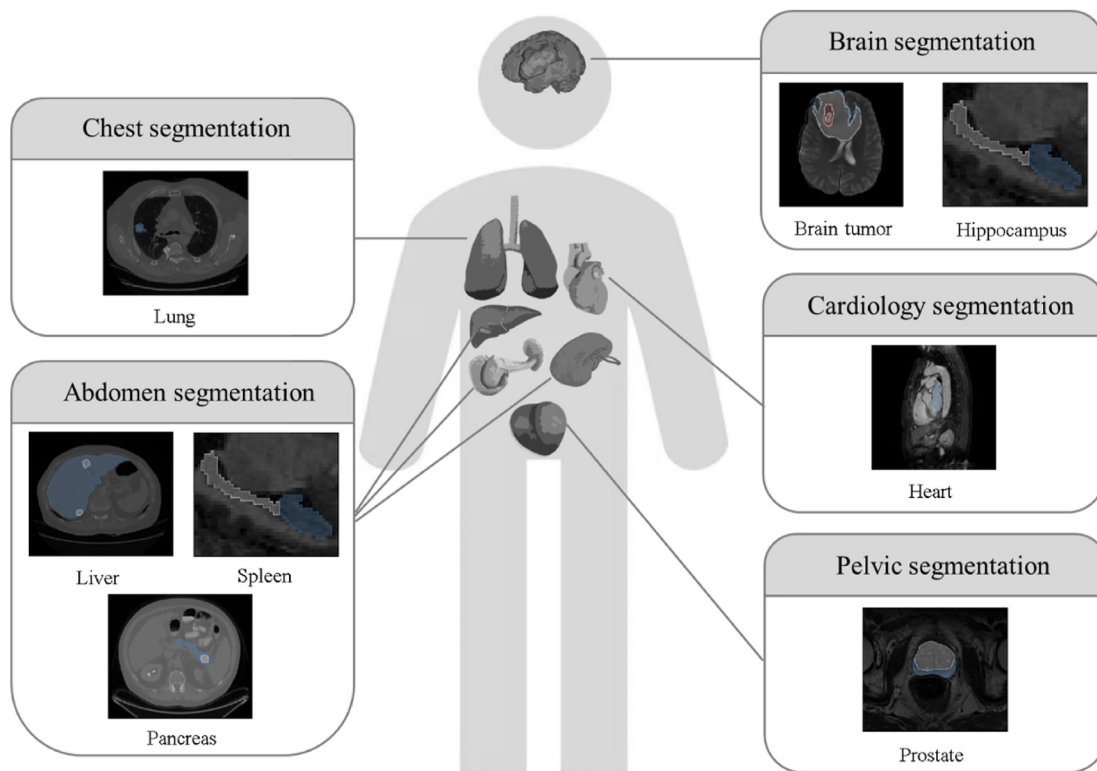


Fig. 1. An example of partial organ segmentation. Image data are obtained from Medical Segmentation Decathlon. (Simpson et al. (2019) [5]).

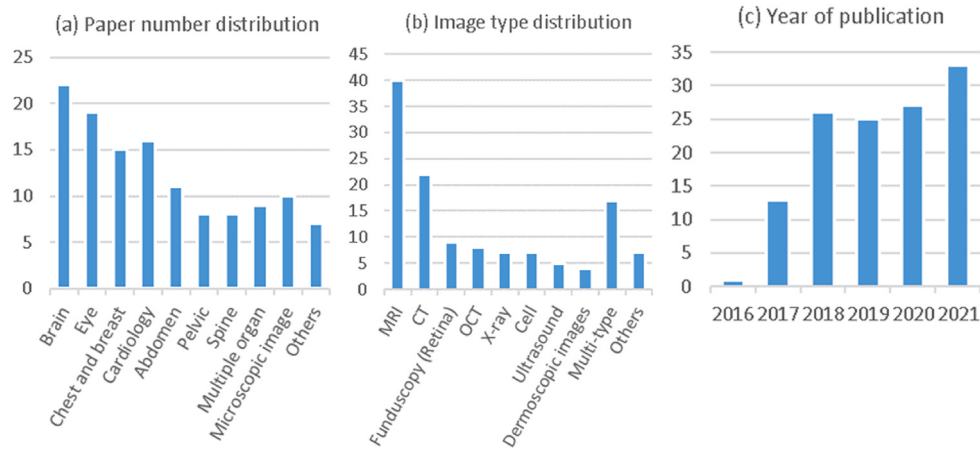


Fig. 2. (a) Categorization of GAN related papers according to segmentation tasks. (b) Categorization of GAN related papers according to imaging modality. (c) Categorization of GAN related papers according to the year of publication.

based on deep learning have made remarkable progress.

This paper focuses on one of the recent breakthroughs in the field of deep learning - Generative Adversarial Network (GAN) (Goodfellow et al. (2014)) [2] - and their potential applications in the field of medical image segmentation. GAN is derived from the zero-sum game of game theory, and it consists of a generator and a discriminator. The network is trained by antagonistic learning to estimate the potential distribution of data samples and generate new data samples. Since it was proposed, the adversarial training scheme has gained attention from both academia and industry because of its usefulness in counteracting domain shifts and the effectiveness in generating new image samples. Although Kazeminia et al. (2019) [3] and Yi et al. (2019) [4] have summarized the application of GAN in medical images, they did not make an in-depth and comprehensive analysis of GAN for medical image segmentation.

This review summarizes more than 120 papers published before September 2021 on GAN-based architectures for medical image segmentation. In this review, the research works were divided into 10 categories according to the segmentation areas including brain, eyes, chest and breast, heart, abdomen, pelvis, bones, multiple organs, microscopy, and other parts. An example of partial organ segmentation is shown in Fig. 1. Meanwhile, the methods based on GAN have been applied to different medical imaging modalities such as Magnetic Resonance Imaging (MRI), Computed Tomography (CT), and Optical Coherence Tomography (OCT). In Fig. 2, these research works were classified in terms of segmentation tasks, imaging modality, and years.

The papers were retrieved by searching on Google Scholar and PubMed with the keywords of “segmentation”, “medical image”, “GAN (or generative adversarial network)”, as well as the above applications.

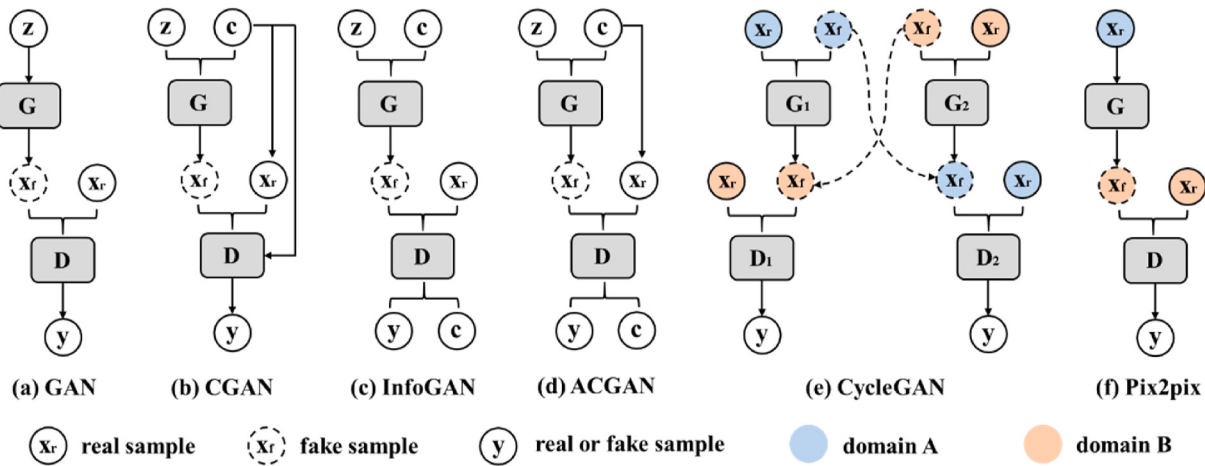


Fig. 3. A schematic view of variants of GAN.

Table 1
Confusion matrix example.

	Positive	Negative
True	True Positive (TP)	True Negative (TN)
False	False Positive (FP)	False Negative (FN)

Table 2
Summary of common evaluation metrics of segmentation model.

Metric name	Formula	Meaning
Accuracy (Acc)	$Acc = \frac{TP + TN}{TP + TN + FP + FN}$	The ratio of the predicted true sample to the total sample number, it used for comprehensive evaluation of segmentation results.
Dice Similarity Coefficient (DSC)	$DSC = \frac{2TP}{2TP + FP + FN}$	It tells about the mutual value among input image and segmented output image.
F-Score	$F - Score = \frac{2PR}{P + R}$	Precision (P) and Recall (R) weighted harmonic average.
Intersection Over Union (IOU)	$JI = IOU = \frac{TP}{TP + FP + FN}$	It used to compare similarities and differences between finite sample sets. The larger the coefficient value, the higher the sample similarity.
Jaccard Index (JI)	$JI = JI = \frac{TP}{TP + FP + FN}$	The ratio of correctly marked pixels to total pixels.
Pixel Accuracy (PA)	$PA = \frac{TP + TN}{TP + TN + FP + FN}$	The ratio of samples predicted to be positive examples that are truly positive.
Precision (Pre)	$Pre = \frac{TP}{TP + FP}$	The ratio of predicted positive examples to all true positive examples, it provided the ability of the test to identify positive results.
Recall (Rec)	$Rec = Sen = \frac{TP}{TP + FN}$	The ratio of predicted negative examples to all true negative examples, it provided the ability of the test to identify negative results.
Sensitivity (Sen)	$Sen = \frac{TP}{TP + FN}$	
Specificity (Spe)	$Spe = \frac{TN}{FP + TN}$	

During the retrieval process, the papers that were not related to GAN and those that did not directly use GAN for image segmentation were excluded. Also, to increase the retrieval scope, more searches were performed on Semantic Scholar, Springer, arXiv, and the top conferences in computer science with the above keywords. Besides, the references and citations of the selected papers were checked.

The remainder of the paper is structured as follows. First, the principles of GAN and some of its extension models are introduced in Section 2. In Section 3, the common evaluation metrics of segmentation models, and the contributions of GAN in medical image segmentation

applications (brain, eyes, chest and breast, heart, abdomen, pelvis, bones, multiple organs, microscopy, and other parts) are described. Finally, the advantages, challenges, and future research directions of GAN in the application of medical image segmentation are discussed in Section 4.

2. Background

This section introduces the principles of GAN and some of the prominent extension models. The extension models include the Conditional Generative Adversarial Networks (CGAN), Deep Convolutional Generative Adversarial Networks (DCGAN), Information Generative Adversarial Networks (InfoGAN), Auxiliary Classifier Generative Adversarial Networks (AC-GAN), Wasserstein Generative Adversarial Networks (Wasserstein-GAN), Cycle Generative Adversarial Networks (CycleGAN), etc.

2.1. GAN

In 2014, Ian Goodfellow and his colleagues at the University of Montreal created GAN. GAN consists of two parts: the discriminator (**D**) and the generator (**G**) (Fig. 3. (a)). The generator mainly learns the real data distribution and produces similar “fake” data. The discriminator discriminates between real data and generated “fake” data, and it gives the result as “real” or “fake”. Meanwhile, the discriminator feeds back the discriminant result to the generator to make the generated data more realistic. Over time, the images generated by the generator are more and more real, and the performance of the discriminator to judge the generated images is higher and higher. Finally, the two parts reach a balance.

Goodfellow et al. (2014) [2] defined two multilayer perceptrons to build an adversarial modeling framework. The first multilayer perceptron $G(z; \theta_g)$ represents the prior on the input noise variable $p_z(z)$ mapping to the data space, where **G** is a differentiable function with parameter θ_g . The generator **G** implicitly defines the probability distribution P_g of the samples $G(z)$ on data X when $z \sim p_z$. Its main goal is to optimize the mapping, i.e., to continuously optimize itself to produce fake data that can fool the discriminator **D**. The second multilayer perceptron $D(x; \theta_d)$ outputs a single scalar, where **D** is a differentiable function with parameter θ_d , and $D(x)$ represents the probability that x comes from the data. Essentially, as a binary classifier, **D** produces $D(x) = 1$ or $D(\hat{x}) = 0$ to classify true and false samples, and it constantly learns to differentiate between real and synthesized samples. In other words, **D** and **G** play a two-player minimax game with the following value function $V(D, G)$:

Table 3

Segmentation GAN-based methods – Brain. List of abbreviations: PPV = positive predictive value; ASSD = average symmetric surface distance; AUPRC = area under the precision-recall curve; NCC = number of connected components; MAD = mean absolute surface distance; MAXD = maximum absolute surface distance; ICC = intraclass correlation coefficient; HD = hausdorff distance.

Paper	Region	Modality	Method	Loss	Data	Performance
Li et al. (2017) [17]	Enhanced tumor, peritumor edema and necrotic non-enhanced tumor	MRI	GAN	Adv, content loss	BraTS 2017 Train: 250 Test: 35	(whole, core, enhanced) DSC = 0.87, 0.72, 0.68 PPV = 0.86, 0.71, 0.68 Sen = 0.87, 0.72, 0.68
Rezaei et al. (2017) [18]	High grade and low grade gliomas of the brain	MRI	CGAN MGAN	Adv	BraTS 2017 Train: 328 Test: unknown	(whole, Core, enhanced) DSC = 0.70, 0.55, 0.40 Sen = 0.68, 0.52, 0.99 Spe = 0.99, 0.99, 0.99
Xue et al. (2018) [19]	The entire tumor, the tumor core, and the GD-enhanced tumor core	MRI	U-Net GAN	Adv, multiscale loss	BraTS 2013 Train: 25 BraTS 2015 Train: 274	(whole, core, enhanced) DSC = 0.84, 0.70, 0.65 Pre = 0.87, 0.80, 0.68 Sen = 0.83, 0.74, 0.72 DSC = 0.85, 0.70, 0.66 Pre = 0.92, 0.80, 0.69 Sen = 0.80, 0.65, 0.62
Yuan et al. (2019) [20]	Glioma	MRI	UAGAN (Unified Attentional GAN)	Adv, cross entropy	Unknown Train: 50 Test: 50	(T1Gd, FLAIR, T2) DSC = 0.5361 ± 0.055, 0.8155 ± 0.0296, 0.7654 ± 0.0291 Pre = 0.6611 ± 0.0302, 0.8120 ± 0.0411, 0.8016 ± 0.0352 Sen = 0.5114 ± 0.0766, 0.8498 ± 0.0192, 0.7745 ± 0.019 Spe = 0.9957, 0.9951, 0.9960 ASSD = 8.46 ± 1.09, 2.53 ± 0.29, 3.44 ± 0.63
Nema et al. (2020) [21]	Whole tumor, core tumor region, enhancing region	MRI	CycleGAN	Adv, cycle consistency loss	BraTS 2015, BraTS 2017 Train: 27 Test: 247	(whole, core, enhanced) DSC = 0.9463, 0.856, 0.9354 Sen = 0.9127, 0.86, 0.9587
Li et al. (2020) [22]	Whole tumor area (WT), tumor core area (TC) and enhancing tumor area (ET).	MRI	U-Net GAN VGG	Adv, cross entropy loss, traditional segmentation loss	BraTS 2017 Train: 228 Test: 57	(whole, core, enhanced) DSC = 0.901, 0.781, 0.682
Conte et al. (2021) [23]	Whole lesion, the FLAIR hyperintensities, and the contrast-enhanced areas	MRI	GAN	Cross-entropy loss, L ₁	BraTS 2017 Train: 135 Test: 42 Validation: 33	(whole, hyperintensities, enhanced) replace both T1-weighted and FLAIR DSC = 0.82, 0.71, 0.92 DSC = 0.84, 0.74, 0.97 replacing T1-weighted DSC = 0.97, 0.95, 0.92
Cheng et al. (2021) [24]	Whole tumor (WT), tumor core (TC), enhancing tumor (ET)	MRI	U-Net GAN	Adv, binary cross entropy loss	BraTS19 Train: Unknown Test: Unknown	(WT, TC, ET) 5% False Label DSC = 0.896, 0.805, 0.763 HD = 5.51, 7.45, 3.92 Sen = 0.910, 0.816, 0.772 Spe = 0.994, 0.996, 0.997 10% false label DSC = 0.891, 0.800, 0.759 HD = 5.62, 7.68, 4.29 Sen = 0.904, 0.810, 0.768 Spe = 0.993, 0.995, 0.996
Moeskops et al. (2017) [25]	Brain tissue	MRI	GAN	Adv, cross entropy	MICCAI 2012 Challenge Train: 15 Test: 20 MRBrainS13 challenge Train: 5 Test: 15	DSC = 0.92 ± 0.03 DSC = 0.85 ± 0.01
Mondal et al. (2018) [26]	White matter, gray matter and cerebrospinal fluid	MRI	U-Net GAN	Adv, cross-entropy, Feature Matching	iSEG-2017 Train: 10 Test: 13 MRBrainS 2013 Train: 5 Test: 15	(WM, GM, CSF) DSC = 0.77, 0.76, 0.89 ASSD = 0.68, 0.72, 0.26 DSC = 0.75, 0.72, 0.55 ASSD = 0.96, 1.10, 2.04
Oh et al. (2020) [27]	White matter	¹⁸ F-FDG PET/ CTMRI	CGAN pix2pix	Adv, L ₁	ADNI Train: 154 Test: 19 Validation: 19	Pre = 0.821 ± 0.036 Rec = 0.814 ± 0.029 DSC = 0.817 ± 0.018 AUPRC = 0.869 ± 0.021
Delisle et al. (2021) [28]	White matter (WM), gray matter (GM) and cerebrospinal fluids (CSF)	MRI	U-Net DCGAN	Adv, dice loss, cross entropy loss	iSEG, MRBrainS, ABIDE Train: 8, 3, 661 Validation: 1, 1, 221 Test: 1, 1, 221	(GM, WM, CSF) DSC = 0.887, 0.870, 0.913 Mean HD = 0.422, 0.598, 0.293

(continued on next page)

Table 3 (continued)

Paper	Region	Modality	Method	Loss	Data	Performance
Zhao et al. (2018) [29]	Craniomaxillofacial bony structure	MRI CT	GAN VGG16	Adv, perceptual loss, voxel-wise	ADNI Train: 16 Test: unknown	DSC = 0.94
Chen et al. (2019) [30]	Craniomaxillofacial bone structure	MRI CT	U-Net CycleGAN	Adv	ADNI Train: 1 Test: 8	DSC = 0.8856 ± 0.0326 ASSD = 1.04 ± 0.19
Shi et al. (2019) [31]	Hippocampus (CA1, CA2, DG, CA3, Head, Tail, SUB, ERC and PHG)	MRI	UG-net	Adv, multi-class cross-entropy, binary classification	CIND Center Train: 27 Test: 5	(CA1, CA2, DG, CA3, Head, Tail, SUB, ERC, PHG, Overall) DSC = 0.919, 0.648, 0.903, 0.673, 0.929, 0.913, 0.906, 0.884, 0.899, 0.916
Delannoy et al. (2020) [32]	Neonatal brain	MRI	GAN	Adv, Reconstruction	dHCP5 Train: 40 French Epirmex Train: 1500 Test: unknown	DSC = 0.855 ± 0.014 NCC = 8.62 ± 3.27
Li et al. (2021) [33]	Neonatal brain	MRI	RES-Unet	Adv, Dice loss, MSE	(NeoBrainS12, dHCP) Train and Test: 7, 10	(dHCP→NeobrainS12 , NeobrainS12→dHCP) DSC = 0.892, 0.878 Sen = 0.891, 0.864 HD = 6.22, 6.24
Alex et al. (2017) [34]	Necrotic areas, edema, non-enhanced tumors and enhanced tumors, ischemic lesions	MRI	GAN	Adv	BraTS Train: 8 ISLES	DSC = 0.69 Sen = 0.91 Spe = 0.59
Kamnitsas et al. (2017) [35]	Abnormalities in brain tissue	MRI(TBI)	GAN 3D CNN	Adv, SGD, cross entropy	Test: unknown unknown 61 + 41	DSC = 0.62 Rec = 0.58 Pre = 0.71
Kuang et al. (2020) [36]	Apoplexy lesions (ischemic, hemorrhage)	NCCT	MPC-GAN (Multi-Path Contextual GAN)	Adv	Unknown ischemic : Train: 60 Test: 60 hemorrhage : Train: 70 Test: 70	(ischemic, hemorrhage) DSC = 0.706 ± 0.124, 0.765 ± 0.129 MAD = 4.3 ± 2.6, 5.7 ± 7.6 MAXD = 11.9 ± 7.1, 41.7 ± 32.1
Finck et al. (2020) [37]	Juxtacortical lesions	MRI	GAN	Adv, cycle consistency reconstruction loss	Unknown Train: 50 Test: 50	(Periventricular, Juxtacortical, Infratentorial, Subcortical) ICC = 0.95, 0.90, 0.87, 0.89
La Rosa et al. (2021) [38]	White matter lesions (WMLs), cortical lesions (CLs)	MRI	Pix2pix	Perceptual loss, cross-entropy loss, L ₁ loss	Unknown Train: 20 Test: 36	(WML, CL) Detection rate = 0.73, 0.72

$$\min_{G} \max_{D} V(D, G) = E_{x \sim p_{\text{data}}(x)} [\log(D(x))] + E_{z \sim p_z(z)} [1 - \log(D(G(z)))] \quad (1)$$

The training of GAN can be regarded as a process of continuously optimizing the above objective function. Since the objective function is composed of two parts, the training can be conducted in two steps:

- 1) Fix generator **G** and update discriminator **D** to maximize the objective function;
- 2) Fix discriminator **D** and update generator **G** to minimize the objective function.

In the process, the backpropagation algorithm is used to update the parameters. Through this min-max optimization process, the following optimization generation model is obtained:

$$G^* = \operatorname{argmin}_{G} \max_{D} V(D, G) \quad (2)$$

2.2. CGAN

CGAN is an extended model of GAN proposed by Mirza and Osindero (2014) [6] (Fig. 3. (b)). In this model, the information *C* is added to both the generator and the discriminator as a condition. *C* can be any information, such as category information or other modal data. CGAN is realized by conveying the additional information *C* to the generation model and discriminant model as part of the input layer. Similarly, the objective function of CGAN is a two-player minimax game with conditional probability:

$$\min_{G} \max_{D} V(D, G) = E_{x \sim p_{\text{data}}(x)} [\log(D(x|c))] + E_{z \sim p_z(z)} [1 - \log(D(G(z|c)))] \quad (3)$$

As a generation confrontation model with conditional constraints,

CGAN can be regarded as an improvement of the unsupervised GAN into the supervised model. This improvement has been proven to be effective, which provides guidance for subsequent works.

2.3. DCGAN

In 2015, Alec Radford proposed a GAN model called DCGAN by combining the success of CNN in supervised learning and unsupervised learning (Radford et al. (2015)) [7]. DCGAN uses the generation model and discriminant model to learn a hierarchical representation from objects to scene images. Finally, the new task is implemented with the learned features – illustrating the representations that they can be used to generate the image. To avoid the reliance on the standard multilayer perceptron architecture, DCGAN uses transposed convolution operation and deconvolution layer.

This is a milestone in the study of GAN because it makes an important architectural change to solve problems such as training instability, pattern collapse, and internal covariant transformation. Since then, DCGAN-based architectures have been widely applied.

2.4. InfoGAN

Although trained GAN can generate new images, they cannot generate images with certain characteristics. In 2016, Chen et al. proposed InfoGAN (Chen et al. (2016)) [8] (Fig. 3. (c)), a GAN that is capable of learning disentangled representation without supervision. Based on information theory, InfoGAN has the potential to solve the explanatory problem of GAN's hidden variables.

The “Info” represents the mutual information between the generated distribution *G(z, c)* and the implicit encoding *c*. To make the correlation

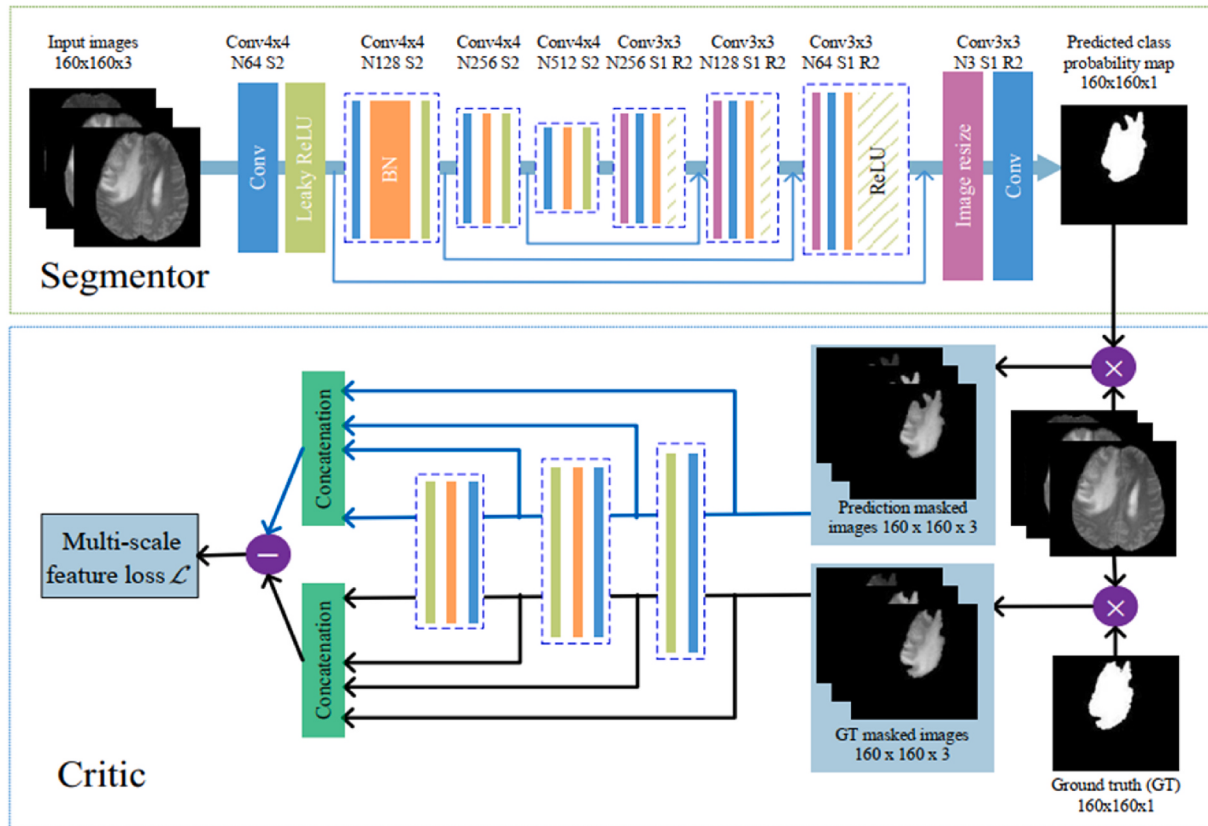


Fig. 4. The architecture of the proposed SegAN to segment brain tumor in Xue et al. (2018) [19].

between x and c close, $I(c; G(z, c))$ should be maximized. Therefore, regular term constraints are added to the original GAN objective function. Meanwhile, an auxiliary distribution $Q(c|x)$ is defined to approach posterior $P(c|x)$, so that the lower bound of the variation of $P(c|x)$ can be obtained. Finally, the objective function can be expressed as:

$$\min_{G, Q} \max_D V_I(D, G, Q) = V(D, G) - \lambda L_I(G, Q) \quad (4)$$

2.5. ACGAN

The ACGAN proposed by Odena et al. (2017) [9] (Fig. 3. (d)) improves the quality of generated data by combining and reconstructing label information. The ACGAN model is class conditional, but it uses an auxiliary decoder to reconstruct the category tags. In ACGAN, the generator G uses the inputs of noise Z and the corresponding category label $C \sim P_C$ to generate sample $X_{fake} = G(c, z)$. The discriminator D gives the discriminant probability of the image's true and false and category labels respectively. Thus, the objective equation contains two parts, as shown below:

$$L_S = E[\log P(S=real|X_{real})] + E[\log P(S=fake|X_{fake})] \quad (5)$$

$$L_C = E[\log P(C=c|X_{real})] + E[\log P(C=c|X_{fake})] \quad (6)$$

The training of the discriminator D maximizes $L_s + L_C$, while the training of the generator G maximizes $L_s - L_C$. In ACGAN, the expression of Z is learned independently of the class tag.

2.6. Wasserstein-GAN

In 2017, Arjovsky et al. proposed Wasserstein GAN (Arjovsky et al. (2017)) [10]. Wasserstein GAN is a thorough solution to the problem of unstable GAN training because there is no need to carefully balance the training level of the generator and discriminator. Meanwhile, it helps to

solve the problem of mode collapse, thus ensuring the diversity of the generated samples. Besides, because of the superior smoothing characteristics of Wasserstein distance to KL divergence and JS divergence, Wasserstein-GAN can theoretically solve the problem of gradient disappearance and provide a reliable training process indicator.

2.7. CycleGAN

CycleGAN (Fig. 3. (e)) was proposed by Zhu et al. (2017) [11], and it is dedicated to solving the problem of image transformation between two domains. It uses two mirror-symmetric GAN to form a ring network to find the mapping between domain X and domain Y. The generator G takes an image from X and tries to map it to Y. The discriminator D_Y determines whether the image is generated by G or Y. Similarly, generator F takes an image from Y and tries to map it to X, and the discriminator D_X determines whether the image is generated by F or whether it exists in X.

To further improve performance, CycleGAN uses the cyclic consistency loss, which is defined as:

$$L(G, F, D_X, D_Y) = L_{GAN}(G, D_Y, X) + L_{GAN}(F, D_X, Y, X) + \lambda L_{cyc}(G, F) \quad (7)$$

$$L_{cyc}(G, F) = E_{x \sim P_{data}(x)} [\| F(G(x)) - x \|_1] + E_{y \sim P_{data}(y)} [\| G(F(y)) - y \|_1] \quad (8)$$

2.8. Pix2pix

Isola et al. (2017) [12] proposed pix2pix (Fig. 3. (f)) as a special CGAN for conversion between different types of images. Pix2pix uses U-net (Ronneberger et al. (2015)) [13] to improve the detail and Markov discriminator (PatchGAN) to process the high-frequency parts of the image. The input of G is a Y-type image y (condition y), and the output is the generated image $G(y)$. The input of D is an X-type image x and a Y-type image y . D needs to determine whether image x is the true image

Table 4

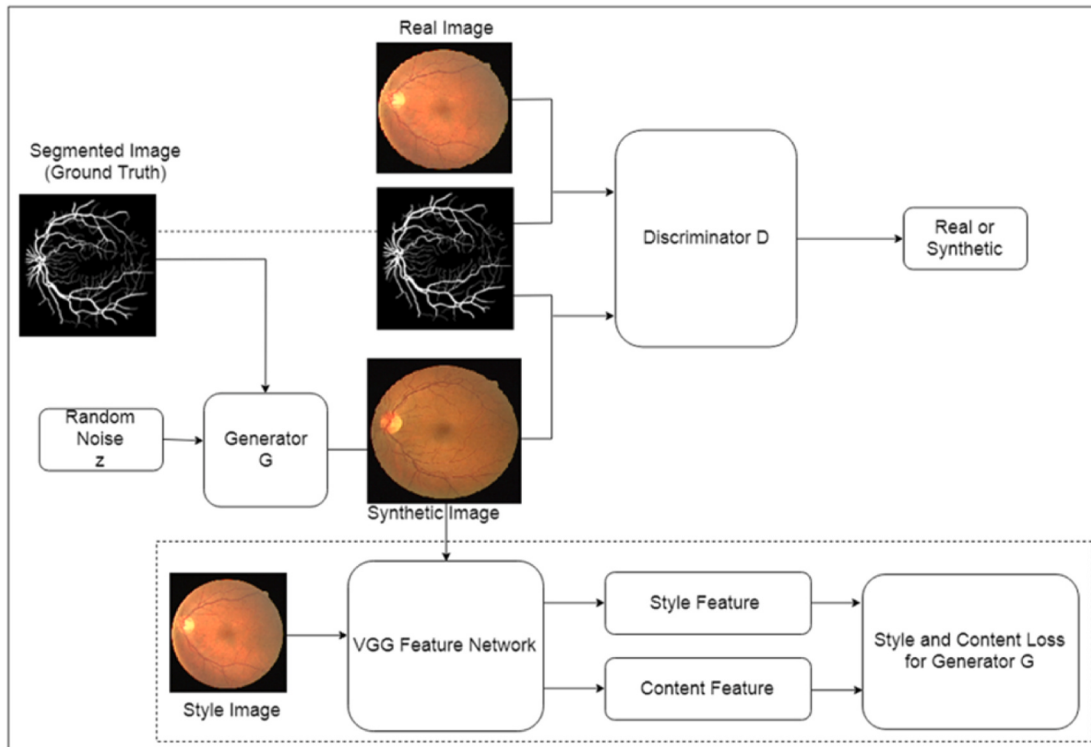
Segmentation GAN-based methods – Eye. List of abbreviations: AUC = area under the receiver operating characteristic curve; CE = contour error; AVD = absolute volume difference; MADLBP = mean absolute difference in layer boundary position.

Paper	Region	Modality	Method	Loss	Data	Performance
Lahiri et al. (2017) [39]	Retinal fundus vessels	Funduscopy (Retina)	DCGAN	Adv, Classification	DRIVE Train: 20 Test: 20	AUC = 0.945
Mahapatra et al. (2017) [40]	Retinal vessel	Funduscopy (Retina)	SRGAN (Super Resolution using GAN)	Adv, Content, Local Saliency	DRIVE, STARE, CHASE Train: 88 Test: unknown	(DRIVE, STARE, CHASE) Acc = 0.96, 0.96, 0.95 Sen = 0.77, 0.87, 0.82
Javanmardi and Tasdizen (2018) [41]	Blood vessels of the eyes	Funduscopy (Retina)	FCN GAN	Adv, Softmax, domain classification	DRIVE, STARE Train: 20, 10	(DRIVE, STARE) F-score = 76.75, 67.09
Iqbal and Ali (2018) [42]	Retinal vessel	Funduscopy (Retina)	MI-GAN (GAN for Medical Imaging)	Adv, binary cross-entropy, perceptual	DRIVE, STARE Train: 20, 10 Test: 20, 10	(DRIVE, STARE) DSC = 0.832, 0.838 AUC = 0.984, 0.985 AUPRC = 0.916, 0.922
Son et al. (2019) [43]	Retinal blood vessels and optic disc	Funduscopy (Retina)	U-Net GAN	Adv, Cross entropy	DRIVE, STARE Train: 20, 10 Test: 20, 10	(DRIVE, STARE) DSC = 0.8275, 0.8378 AUC = 0.9810, 0.9873 AUPRC = 0.9145, 0.9226
Yang et al. (2020) [44]	Retinal vessel	Funduscopy (Retina)	SUD-GAN (Segmentation model based on DCGAN)	Adv, binary cross entropy, pixel-level	DRIVE, STARE Train: 20, 10 Test: 20, 10	(DRIVE, STARE) Acc = 0.9560, 0.9663 Sen = 0.8340, 0.8334 Spe = 0.9820, 0.9897 AUC = 0.9786, 0.9734 AUPRC = 0.8821, 0.8718
Schlegl et al. (2017) [45]	Fundus abnormalities (retinal fluid or overreaction lesions)	OCT	AnoGAN (Anomaly Detection with GAN)	Adv, Residual, Discrimination	Unknown Train: 270 Test: 20	Pre = 0.8834 Rec = 0.7277 Sen = 0.7279 Spe = 0.8928 AUC = 0.89
Jiang et al. (2019) [46]	Backgrounds, linear lesions and retinal vessels	ICGA	CGAN PatchGAN	Adv, L ₁ , Dice, Binary cross-entropy	Unknown Train: 38 Test: unknown	IOU = 0.5295 ± 0.0122 DSC = 0.6921 ± 0.0104 Acc = 0.9892 ± 0.0034 Sen = 0.7763 ± 0.0223 Spe = 0.9929 ± 0.0026
Schlegl et al. (2019) [47]	Retinal abnormality	OCT	WGAN	Adv, mean squared error residual loss	Unknown Train: 270 Test: 20	Pre = 0.7863 Sen = 0.8091 Spe = 0.9049 F-score = 0.7975 AUC = 0.9301
Wang et al. (2021) [48]	Retinal anomaly	OCT	CycleGAN	Adv, MS-SSIM loss, L ₁ loss	K's dataset, Chiu's dataset Train: 21656, 0 Test: 750, 78	AUC = 0.9694 DSC = 0.8239 Pre = 0.9671 Sen = 0.8374 F-score = 0.8976 Spe = 0.7864
Shankaranarayana et al. (2017) [49]	Optic cup and optic disc	Funduscopy (Retina)	CGAN ResU-net	Adv, L ₁	RIM-ONE Train: 159 Test: unknown	(disc, cup) F-score = 0.97, 0.94 IOU = 0.89, 0.76
Wang et al. (2019) [50]	Optic cup and optic disc	Funduscopy (Retina)	DeepLabv3+ MobileNetV2 GAN	Joint morphological Adv	Drishti-GS, RIM-ONE-r3, REFUGE Train: 50, 99, 400 Test: 51, 60, 400	(Drishti-GS, RIM-ONE-r3, REFUGE) DSC (cup) = 0.858, 0.787, 0.875 DSC (disc) = 0.965, 0.865, 0.946 δ = 0.082, 0.081, 0.051

(continued on next page)

Table 4 (continued)

Paper	Region	Modality	Method	Loss	Data	Performance
Kadambi et al. (2020) [51]	Optic cup and optic disc	Funduscopy (Retina)	WGAN	Adv, cross-entropy	REFUGE, Drishti-GS1 Train: 400, 101 Test: unknown	(disc, cup) IOU = 0.912, 0.724 DSC = 0.954, 0.840
Luo et al. (2021) [52]	Optic cup (OC) and optic disc (OD)	OCT	MobileNetv2 GAN	Adv, binary cross entropy loss	Drishti-GS, RIM-ONE-r3, REFUGE Train: 40 Validation: 40 Test: 40	(Drishti-GS, RIM-ONE-r3, REFUGE) OC: DSC = 0.898, 0.872, 0.8658 OD: DSC = 0.975, 0.967, 0.9514
Liu et al. (2018) [53]	Inner layer and fluid area of the retina	OCT	SGNET (Semi-supervised segmentation with GAN)	Adv, Multi-class cross entropy, Dice overlap	Duke, POne Train: 10 Test: 10	(Duke, POne) DSC = 0.900, 0.929 CE = 1.068, 0.695
Tennakoon et al. (2018) [54]	Retinal fluid	OCT	U-Net GAN	Adv, Cross-entropy, Dice	ReTOUCH Train: 52 Test: 18	DSC = 0.75 AVD = 0.11
Jiang et al. (2018) [55]	Lacquer crack	ICGA	CGAN	Adv, Dice, L ₁	Unknown Train: 22 Test: 6	IOU = 0.4738 PA = 0.6959
OuYang et al. (2019) [56]	Cornea, limbus cornea	OCT	CGAN	Adv, L ₁ , MSE	Unknown Train: 45 Test: 5	HD = 1.0335e-04 MADLPB = 0.0344
Yildiz et al. (2021) [57]	Corneal subbasal nerves	In vivo confocal microscopy	U-Net GAN PatchGAN	Adv	Unknown Train: 403 Test: 102	AUC = 0.9439

**Fig. 5.** The schematic diagram of retinal vascular segmentation process proposed in Iqbal and Ali (2018) [42].

of y , and it outputs a probability. The model loss includes L_1 loss and CGAN loss. It is found through experiments that adding L_1/L_2 loss in the generated image and real image can accelerate the convergence of the model and improve the accuracy.

2.9. BigGAN

To successfully generate high-resolution and diversified samples from complex data sets, Brock et al. (2018) [14] proposed BigGAN. This is the first time that GAN can generate images with high fidelity and low variety gap. To this end, the authors train GAN at the largest scale yet attempted, and they study the instabilities specific to such scale. They

found that applying orthogonal regularization to the generator is amenable to a simple “truncation trick,” which allows fine control over the trade-off between sample fidelity and variety and reduces the variance of the generator’s input. This modification makes BigGAN a new state-of-the-art in class-conditional image synthesis. The results show that BigGAN increases the initial value and initial distance.

2.10. StyleGAN

StyleGAN (Karras et al. (2019)) [15] is a result of NVIDIA Research Institute. Contrary to the traditional study of GAN, this study focused on loss function, stability, architecture, etc. Thus, rather than creating more

Table 5

Segmentation GAN-based methods – Chest and breast. List of abbreviations: MSSD = mean symmetric surface distance; RMSD = residual mean square deviation; AvgD = average distance; MCC = matthews correlation coefficient; SSIM = Structural similarity index; NCCC = Normalized cross-correlation coefficient.

Paper	Region	Modality	Method	Loss	Data	Performance
Zhu et al. (2016) [58]	Breast lumps	Mammogram	FCN-CRF GAN	Adv, Empirical	INBreast Train: 58 Test: 58 DDSM-BCRP Train: 39 Test: 40	(INBreast, DDSM-BCRP) DSC = 0.9097, 0.9130
Shen et al. (2019) [59]	Breast lumps	X-ray	CGAN	Adv, L ₁	INbreast, Unknown Train: 63, 180 Test: 49, 196	(INbreast, Unknown) Sen = 92.00, 97.25 Spe = 91.55, 81.84 JI = 80.43, 75.30 DSC = 88.81, 85.41 Overall accuracy = 91.45, 86.17 MCC = 82.24, 73.23
Han et al. (2020) [60]	Breast lesions	Breast ultrasound	BUS-GAN (Breast Ultrasound with GAN)	Adv, Supervised segmentation	Unknown Train: 2000 Test: 963	(Dataset A, Dataset B) DSC = 0.8712, 0.7982 JI = 0.7762, 0.6803 Pre = 0.7762, 0.6803 HD (pixels) = 77.62, 68.03 AvgD (pixels) = 5.364, 9.089
Xing et al. (2020) [61]	Breast lesions	Breast ultrasound	SPGAN (semi-pixel-wise cycle GAN)	Adv, Cycle, Pixel-wise classification	Unknown Train: 399 Test: 241 Validation: 100	DSC = 0.92 ± 0.04
Ma et al. (2020) [62]	Fibrous glandular tissue	MRI (3D)	U-Net GAN	Adv, Dice, Binary cross-entropy	Unknown Train: 100 Test: unknown	DSC = 0.870 ± 0.07 JI = 0.776 ± 0.101
Li et al. (2021) [63]	Breast mass	Mammogram	CGAN	Adv, dice loss	CBIS-DDSM, INbreast Train: 1318, 5272 Test: 378, 106	(CBIS-DDSM, INbreast) DSC = 0.9337, 0.9154 JI = 0.8757, 0.8440 Acc = 0.9835, 0.9855 Spe = 0.9846, 0.9863 Sen = 0.9750, 0.9771
Chen et al. (2018) [64]	Left lung, right lung	X-ray	SeUDA (Semantic-aware GAN for unsupervised domain adaptation)	Adv, Cycle consistency, Semantic-aware	Montgomery Train: 97 Test: 27 Validation: 14 JSRT Train: 173 Test: 49 Validation: 25	(Right lung, Left lung) DSC = 0.9559, 0.9342 Rec = 0.9655, 0.9240 Pre = 0.9477, 0.9470 ASSD = 2.85, 3.51
Tan et al. (2021) [65]	Lung	CT	GAN	EM distance-based loss, Adv, Binary Cross Entropy loss	LIDC-IDRI, Quantitative Imaging Network Train: 180, 35 Test: 40, 12	(LIDC-IDRI, Quantitative Imaging Network) IOU = 0.923, 0.938 HD = 3.380, 2.679
Stiehl et al. (2021) [66]	Lung lobes	CT	CGAN Pix2Pix	Adv, binary cross entropy loss	Unknown Train: 12 Test: 10	SSIM = 0.929 NCCC = 0.806 DSC = 0.814
Jin et al. (2018) [67]	Pulmonary nodules	CT	3D CGAN	Adv, L ₁ , Reconstruction	LIDC Train: 1018 Test: 22	DSC = 0.989 HD = 2.4 ASSD = 1.2
Jain et al. (2021) [68]	Lung nodule	CT	GAN	Adv	LIDC-IDRI Train: Unknown Test: Unknown	DSC = 0.7986 Acc = 0.9387 JI = 0.8026
Dai et al. (2018) [69]	Heart, lung, pleura, etc	X-ray	SCAN (Structure Correcting Adversarial Network)	Adv, Multi-class Cross-entropy, Binary logistic, pixel-wise	JSRT Train: 209 Test: 38 Montgomery Train: 138 Test: unknown	(Lungs, Heart) DSC = 0.973, 0.927 IOU = 0.947, 0.866
Trullo et al. (2019) [70]	Esophagus, heart, trachea and aorta	CT	PatchGAN FCN	Adv, Binary cross entropy	AAPM Train: 40 Test: 20	(Esophagus, Heart, Trach, Aorta) DSC = 0.55 ± 0.13, 0.66 ± 0.10, 0.63 ± 0.10, 0.76 ± 0.07 MSSD = 3.06 ± 0.41, 32.97 ± 11.27, 6.93 ± 0.53, 4.29 ± 0.49
Dong et al. (2019) [71]	Left and right lungs, spinal cord, esophagus, and heart	CT (2D, 3D)	U-Net GAN	Adv, Binary cross entropy, Residual	2017 AAPM Thoracic Auto-segmentation Challenges Train: 34 Test: 1	(Esophagus, Heart, Left lung, Right lung, Spinal cord) DSC = 0.75 ± 0.08, 0.87 ± 0.05, 0.97 ± 0.01, 0.97 ± 0.01, 0.90 ± 0.04 Sen = 0.74 ± 0.10, 0.89 ± 0.07, 0.97 ± 0.02, 0.96 ± 0.02, 0.93 ± 0.03 Spe = 0.9997 ± 0.0001, 0.9977 ± 0.0020, 0.9989 ± 0.0010, 0.9992 ± 0.0007, 0.9998 ± 0.00001 HD = 4.52 ± 3.81, 4.58 ± 3.67, 2.07 ± 1.93, 2.50 ± 3.34, 1.19 ± 0.46 MSSD = 1.05 ± 0.66, 1.49 ± 0.85,

(continued on next page)

Table 5 (continued)

Paper	Region	Modality	Method	Loss	Data	Performance
Guo et al. (2020) [72]	Chest muscle	Mammogram	U-Net GAN	Adv	Unknown Train: 633 Test: 65	$0.61 \pm 0.73, 0.65 \pm 0.53, 0.38 \pm 0.27$ $\text{RMSD} = 2.24 \pm 1.36, 3.14 \pm 2.19, 2.12 \pm 2.32, 2.66 \pm 2.46, 0.82 \pm 0.85$ (Dataset 1, Dataset 2) $\text{DSC} = 0.9703, 0.9622 \pm 0.0495$

realistic images, StyleGAN improves GAN's ability to perform fine-grained control over the resulting images, such as blending images, changing details at multiple levels, and performing more advanced transformations. To achieve this improvement, StyleGAN uses existing techniques such as adaptive instance normalization, potential vector mapping networks, and continuous learning input.

3. Application

GAN has made breakthroughs in image classification, object detection, high-resolution image generation, and many other fields. As for medical image segmentation, GAN makes the segmentation results more continuous and efficiently solves the problem that the segmentation results of an image are quite different from the gold standard. The paper "Semantic Segmentation using Adversarial Networks" (Luc et al. (2016)) [16] is the first to apply the adversarial network to image segmentation tasks. In the following subsections, the common evaluation metrics of the segmentation models are summarized, and the GAN-based segmentation approaches are categorized based on specific parts of the anatomy.

3.1. Evaluation metrics

The accuracy of a segmentation model is an important factor for evaluating the model performance. Ideally, various evaluation metrics should be used to comprehensively evaluate the model. For example, pixel-based evaluation metrics include Precision, Recall, Sensitive, Accuracy, Specificity, F-Score, Pixel Accuracy; overlap-based evaluation metrics include Dice Similarity Coefficient and Jaccard Index.

To make it easier to understand, the studies in this field usually use a matrix, called confusion matrix, to show the difference between the predicted results and the actual ones. As shown in Table 1, where:

- True Positive (TP): Indicates that the sample is predicted as a positive sample, and the prediction is true, that is, the true value is a positive sample
- True Negative (TN): Indicates that the sample is predicted as a negative sample, and the prediction is true, that is, the true value is a negative sample
- False Positive (FP): Indicates that the sample is predicted as a positive sample, but the prediction is false, that is, the true value is a negative sample
- False Negative (FN): Indicates that the sample is predicted as a negative sample, but the prediction is false, that is, the true value is a positive sample.

The common evaluation metrics are summarized in Table 2.

3.2. Application of different parts segmentation

3.2.1. Brain

Brain tissue and brain abnormality segmentation is a popular research field in medical image processing. It differentiates diseased tissue from healthy tissue, thus providing detailed quantitative brain analysis for accurate disease diagnosis and abnormal detection and

classification. Table 3 summarizes the GAN-based segmentation methods and the similarities and differences of brain anatomical regions.

The brain tumor is the most common malignant tumor of the central nervous system. Li et al. used the GAN-based method to effectively segment brain tumors in Refs. [17–24]. In these research works, Xue et al. (2018) [19] took U-net as GAN's generator and proposed multi-scale L1 loss to achieve direct and effective segmentation of brain tumors. The specific network structure is shown in Fig. 4. Conte et al. (2021) [23] used GAN to synthesize missing MRI sequences and proved that the images generated by GAN can effectively assist other deep learning models in segmentation. Cheng et al. (2021) [24] used GAN to perform reweighting and label correction on samples, which improved the image quality of manually segmented labels and further improved the accuracy of brain tumor segmentation.

Moeskops et al. used GAN for brain tissue segmentation (such as gray matter, white matter, etc.) [25–28]. Mondal et al. (2018) [26] first applied GAN to semi-supervised segmentation of 3D multimodal brain images, and the segmentation performance was significantly improved compared with the fully supervised method. Oh et al. (2020) [27] used CGAN with a pix2pix framework to segment the white matter in 18F-FDG PET/CT images, which achieved high-precision brain tissue segmentation.

Based on GAN, Zhao et al. (2018) [29] and Chen et al. (2019) [30] realized accurate segmentation of craniomaxillofacial (CMF) bony structures for MRI and CT images. Shi et al. (2019) [31] proposed UG-net (GAN with the modified U-net) for the segmentation of the hippocampal subfields. Delannoy et al. (2020) [32] and Li et al. (2021) [33] used GAN to segment neonatal brain images, providing help for neonatal disease diagnosis. Besides, GAN-based methods have been adopted to segment other brain lesions and abnormalities effectively [34–38].

3.2.2. Eye

Due to the limitation of fundus image acquisition technology, there is often a lot of noise in the image, coupled with the complex and changeable structure of the retina itself. This makes the segmentation of fundus images difficult. Many GAN-based methods perform even better in fundus image segmentation than human experts. Table 4 summarizes the GAN-based segmentation methods and the similarities and differences of eye anatomical regions.

Automatic segmentation of fundus images is very challenging because the vessels in fundus images have complex branching patterns and there is a lot of noise in the background. Lahiri et al. performed precise segmentation of retinal blood vessels in Refs. [39–44]. Lahiri et al. (2017) [39] used GAN semi-supervised learning for the first time to effectively segment retinal blood vessels. As shown in Fig. 5, Iqbal and Ali (2018) [42] re-defined a set of loss functions to produce a more realistic retinal image and to assist the segmentation task. Yang et al. (2020) [44] improved the network structure of the generator and discriminator, to accurately segment the details of the vessel's edge.

Schlegl et al. segmented abnormal lesions in fundus images [45–48], which provided help for diagnosing ocular diseases. Schlegl et al. (2019) [47] proposed fast AnoGAN, to effectively identify abnormal images and perform image segmentation. Wang et al. (2021) [48] proposed a

Table 6

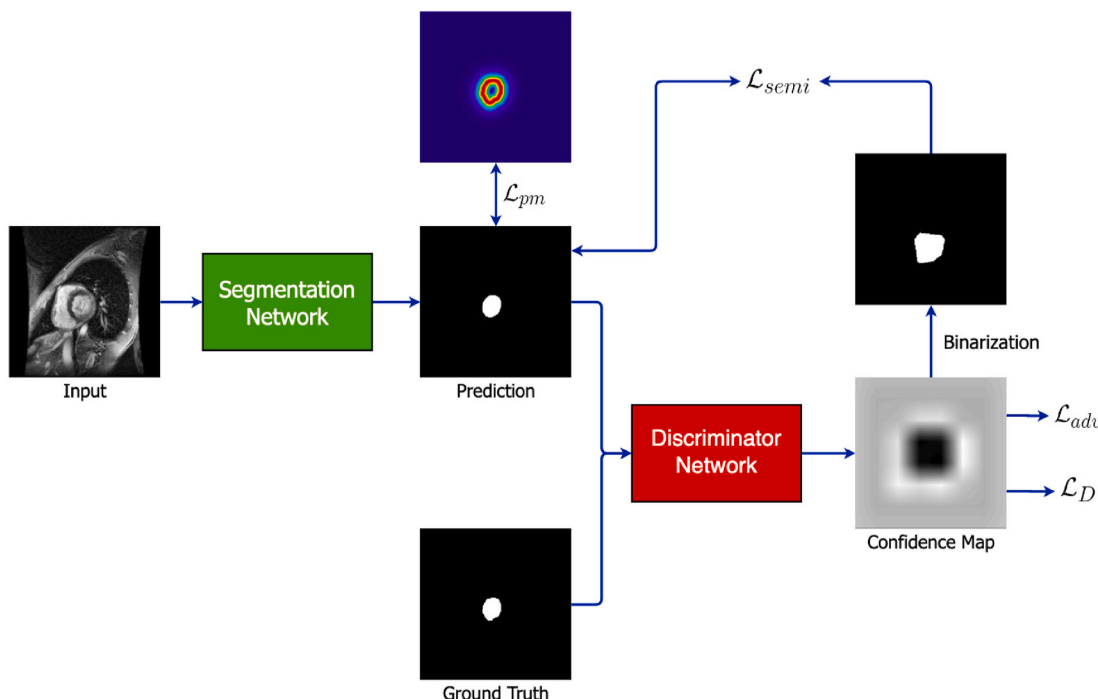
Segmentation GAN-based methods – Cardiology. List of abbreviations: ABD = average boundary distance; HSD = hausdorff surface distance; corr-of-EF = correlation of ejection fractions; APD = average perpendicular distance; PGC = percent of good contours.

Paper	Region	Modality	Method	Loss	Data	Performance
Dou et al. (2018) [73]	Ascending aorta (AA), left atrial blood chamber (LA-blood), left ventricular blood chamber (LV-blood), and left ventricular myocardium (LVmyo)	CT MRI	ConvNets GAN	Adv, Multi-class cross-entropy, Dice coefficient	MICCAI 2017 Multi-Modality Whole Heart Segmentation Train: 16 Test: 4	(AA, LA-blood, LV-blood, LV-myof) DSC = 0.748 ± 0.062, 0.552 ± 0.229, 0.572 ± 0.124, 0.478 ± 0.058 ASSD = 13.9 ± 5.6, 15.2 ± 8.2, 18.4 ± 5.1, 14.2 ± 5.3
Rezaei et al. (2018) [74]	Myocardium tissue and the blood pool	CMRI	CGAN	Adv, L ₁	MICCAI 2016 HVSMR Train: 24 Test: unknown	(myocardium tissue, blood pool) ABD = 1.02, 0.87 DSC = 0.80, 0.93 Sen = 0.87, 0.90 Spe = 0.96, 0.99
Zhang et al. (2018) [75]	The endocardium of the four Chambers and the epicardium of the left ventricle	CT MRI	CycleGAN	Cycle-consistency, discriminative, shape-consistency, cross-entropy loss	Unknown Train: 2177 Test: 2177	(CT, MRI) DSC = 74.4, 73.2
Joyce et al. (2018) [76]	Left ventricle, Right ventricle, and myocardium	CT MRI	U-Net GAN	Adv, Intensity-Var, Over-segpenalty, Recons	MICCAI 2017 Multi-Modality Whole Heart Segmentation Train: 20 Test: 3 MR, 3CT	(CT, MRI) DSC = 0.5, 0.66
Dong et al. (2018) [77]	3D Left ventricle	MRI	VoxelAtlasGAN (voxel-to-voxel) CGAN	Adv, intensity, label	Unknown Train: 25 Test: 35	DSC = 0.95 MSSD = 1.85 HSD = 7.26 corr-of-EF = 0.91
Chartsias et al. (2018) [78]	Myocardial	Cine MR 3D	U-Net GAN	Adv, Reconstruction, Supervised	ACDC, QMRI Train: 128 Test: 50	(ACDC, QMRI) DSC = 0.771, 0.794
Liu et al. (2019) [79]	Myocardium, endocardium, epicardium	CMR	CGAN	Adv, Structured	Unknown Train: 32 Test: unknown	(endocardium, myocardium, epicardium) DSC (DE) = 0.8791 ± 0.0447, 0.7813 ± 0.0622, 0.9262 ± 0.0240 DSC (T2) = 0.9048 ± 0.0382, 0.8497 ± 0.0415, 0.9353 ± 0.0222
Upendra et al. (2019) [80]	Left ventricle	CMRI	U-Net GAN	Adv, L ₁ loss, cross entropy loss	ACDC 2017 Train: 80 Test: 20	(end diastole, end systole) DSC = 0.9587, 0.9314 IOU = 0.9294, 0.8894
Xu et al. (2020) [81]	Myocardial infarction area	MRI	DSTGAN (Deep spatiotemporal adversarial network)	Adv, Multi-task generation, Reciprocal	Unknown Train: 165 Test: unknown	DSC = 0.9289 ± 0.0033 IOU = 0.8216 ± 0.0027
Decourt and Duong (2020) [82]	Myocardium, endocardium, epicardium	MRI	GAN	Adv, Spatial cross-entropy, Pixel-wise cross-entropy, Masked cross-entropy	York, ACDC Train: 25 Test: 4 Validation: 4	(endocardium, epicardium, myocardium) HD = 2.16 ± 0.42, 2.23 ± 0.35, 2.98 ± 0.43 DSC = 0.88 ± 0.08, 0.93 ± 0.04, 0.79 ± 0.10
Shi et al. (2020) [83]	Coronary arteries	Coronary angiography	U-Net CGAN	Binary Cross Entropy Loss, Feature Matching Loss, Content Loss	Unknown Train: 3486 Test: 387	(CRA, RIGHT) DSC = 0.8353, 0.8047
Cui et al. (2021) [84]	Ascending aorta (AA), left atrium blood cavity (LAC), left ventricle blood cavity (LVC)	CT MRI	CycleGAN	Cross-entropy loss, Dice loss, Knowledge distillation loss, Adv	MICCAI 2017 Multi-Modality Whole Heart Segmentation (MRI, CT) Train: 20, 20 Test: 40, 40	(CT, MRI) DSC = 0.815, 0.592 ASSD = 5.8, 4.9
Wu et al. (2021) [85]	Left ventricular	MRI	GAN	Dice loss, Adv	MICCAI 2009 and 2017 challenge Train: 30, 100 Test: 15, 50	(Endocardial, epicardial) 2009: APD = 1.71, 1.64 PGC = 0.9734, 0.9821 2017:

(continued on next page)

Table 6 (continued)

Paper	Region	Modality	Method	Loss	Data	Performance
Yang et al. (2021) [86]	Left ventricle (LV), right ventricle (RV), and myocardium (MYO)	CMRI	U-Net GAN	Binary-class cross-entropy loss, multi-class cross-entropy loss	ACDC Train: 70 Validation: 30 Test: 50	APD = 1.74, 1.70 PGC = 0.9721, 0.9813 (LV, RV, MYO) end-diastolic DSC = 0.96, 0.92, 0.87 HD = 7.6, 10.3, 8.2 end-systolic DSC = 0.88, 0.90, 0.89 HD = 10.8, 12.7, 8.8
Chen et al. (2021) [87]	Left atrium (LA) and atrial scars	CMRI	GAN	Adv, dice loss, cross-entropy loss	Unknown Train: 77 Test: 38	(LA and atrial scars) DSC = 0.946 ± 0.015, 0.821 ± 0.059 JI = 0.897 ± 0.026, 0.700 ± 0.081 ASSD = 0.918 ± 0.460, 0.439 ± 0.232
Gilbert et al. (2021) [88]	Left ventricle (LV) and left atrium (LA)	Ultrasound	CycleGAN U-Net	Adv, cross entropy loss	Camus, EchoNet, Unknown1, Unknown2 Train: 1280, 8020, 269, 0 Validation: 160, 1002, 67, 0 Test: 160, 1002, 229, 122	(LV, LA) DSC = 0.914, 0.830

**Fig. 6.** The architecture to segment heart proposed in Decourt and Duong (2020) [82].

CycleGAN-based weakly supervised learning network for the segmentation of lesions in OCT images. Glaucoma is also one of the most common eye diseases. An important criterion for judging glaucoma is the cup-to-disc ratio (CDR), which requires accurate segmentation of the optic cup and optic disc. Shankaranarayana et al. used different adversarial learning methods to solve this problem [49–52].

Different from the above studies, Liu et al. (2018) [53] and Tenna-koon et al. (2018) [54] used GAN to segment the layer and fluid regions in OCT images; Jiang et al. (2018) [55] applied CGAN and Dice loss function to lacquer cracks segmentation for the first time; Ouyang et al. (2019) [56] and Yildiz et al. (2021) [57] used different GAN-based method to segment the cornea.

3.2.3. Chest and breast

Chest and breast X-rays are one of the most common medical diagnosis techniques. It uses very small doses of rays to produce images of the chest and breast at a low cost and a high speed, which helps diagnose and monitor the treatment of various cardiopulmonary diseases. Table 5 summarizes the GAN-based segmentation methods and the similarities and differences of chest and breast anatomical regions.

Breast cancer is one of the most common cancers, with the highest incidence in females. Zhu et al. segmented breast masses accurately [58–63], which is a prerequisite for computer-aided breast cancer diagnosis. Shen et al. (2019) [59] introduced CGAN to generate X-ray breast mass images and added U-net to improve segmentation accuracy.

Table 7

Segmentation GAN-based methods – Abdomen.

Paper	Region	Modality	Method	Loss	Data	Performance
Yang et al. (2017) [89]	Liver	CT (3D)	DI2IN GAN	Adv, Cross-entropy	MICCAI (SLiver07) Train: 20 Test: 10 Unknown Train: 1000+ Test: unknown	DSC = 0.95 ASSD = 1.90
Kim and Ye (2018) [90]	Liver, lesion area	CT (3D)	U-Net CycleGAN	CycleGAN, Cross entropy, L ₂	LiTS2017 Train: 73 Test: 9	(liver, lesion) DSC = 0.89, 0.46 Rec = 0.94, 0.5 Pre = 0.86, 0.48
Huo et al. (2018) [91]	Spleen	MRI(2D)	CGAN PatchGAN	Adv, Dice	Unknown Train: 45 Test: 15	DSC = 0.9260
Huo et al. (2018) [92]	Splenomegaly	CT MRI	CycleGAN ResNet PatchGAN	Adv, Cycle consistency, Segmentation	Unknown Train: 79 Test: unknown	DSC = 0.9188
Liu et al. (2019) [93]	Colorectal tumor	CT	LAGAN	Adv	Unknown Train: 223 Test: unknown	DSC = 0.9154 ± 0.0053
Poorneshwaran et al. (2019) [94]	Colon polyps	Colonoscope image	Pix2pix CGAN	Adv	CVC-Clinic Train: 488 Test: 62 Validation: 62	JI = 0.8127 DSC = 0.8848
Ruan et al. (2020) [95]	Kidney cancer	CT	MB-FSGAN (Multi-branch feature sharing GAN)	Adv, SoftMax, Smooth L ₁ , Cross-entropy	Unknown Train: 70 Test: 20 Validation: 23	PA = 0.957 DSC = 0.859 Spe = 0.894 Sen = 0.862
Huang et al. (2021) [96]	Stomach	MRI	CycleGAN 3D Res-Unet PatchGAN	Adv, Dice	Unknown Train: 10 Test: 4 Validation: 2	DSC = 0.690, 0.722 HD = 8.04, 7.97 Sen = 0.602, 0.594 Spe = 0.999, 0.999
Li et al. (2021) [97]	Pancreas	CT	GAN U-Net	Adv	NIH pancreas dataset Train: 62 Test: 20	DSC = 0.8393 ± 0.063 JI = 72.61 ± 8.48
Sandfort et al. (2019) [98]	Kidney, liver and spleen	CT	CycleGAN	Adv, dice loss	NIH Pancreas-CT, Liver Data Decathlon, Spleen Data Decathlon Train: 50, 179, 30 Test: 13, 43, 8 Validation: 3, 9, 2	(contrast CT, non-contrast CT) DSC = 0.932, 0.747
Conze et al. (2021) [99]	Liver, right kidney, left kidney, spleen, multi-organ	CT MRI	U-Net CGAN	Adv, dice loss	CHAOS Train: 40 Test: 40	(liver, right kidney, left kidney, spleen, multi-organ) F-score = 85.53, 70.17, 70.39, 64.77, 69.92, 68.78

Xing et al. (2020) [61] combined CycleGAN and FCN to segment breast lesions, which relieves the radiologists' burden for annotation.

Pulmonary segmentation is crucial for in the diagnosis of various pulmonary diseases. Chen et al. (2018) [64], Tan et al. (2021) [65], and Stiehl et al. (2021) [66] performed segmentation of lungs in different medical images. Specifically, Tan et al. (2021) [65] combined EM distance-based loss function with GAN to perform accurate lung segmentation of the input CT scans. Among all kinds of lung diseases, lung cancer is one of the most common causes of death. Jin et al. (2018) [67] added a novel multi-mask reconstruction loss in GAN to generate more realistic pulmonary nodule images. To accurately detect the presence of lung cancer, Jain et al. (2021) [68] improved the GAN model by using the salp shuffled shepherd optimization algorithm for lung nodule segmentation.

In addition, Dai et al. used different GANs to perform automatic segmentation of multiple thoracic organs at risk [69–71], providing great convenience for the development of radiotherapy plans. Guo et al. (2020) [72] used U-net for boundary recognition and GAN for shape prediction to segment pectoral muscle regions.

3.2. 4. Cardiology

The segmentation of the heart in medical images is more complicated than other regions. This is because the heart is a constantly working organ and its shape changes during exercise. Therefore, accurate calculation, modeling, and analysis of the entire heart structure are of great importance for research and application in the medical field.

Table 6 summarizes the GAN-based segmentation methods and the similarities and differences of cardiology anatomical regions.

Due to the different shapes and working modes of each region in the heart, the segmentation methods and difficulties of each region are also different. Based on this, Dou et al. segmented different regions of interest in Refs. [73–88].

Meanwhile, Xu et al. (2020) [81] proposed a deep spatiotemporal adversarial network to realize synchronous segmentation and quantification of the myocardial infarction area. As shown in Fig. 6, Decourt and Duong (2020) [82] proposed a new loss function to segment boundary pixels more accurately and effectively improve the segmentation accuracy of the myocardium, endocardium, and epicardium in the case of limited annotation data. Shi et al. (2020) [83] used U-net and a pyramid structure as the generator and discriminator respectively to extract fine features of coronary arteries. Yang et al. (2021) [86] proposed a dilated block adversarial network to segment the left ventricle, right ventricle, and myocardium in short-axis cardiac MRI; Chen et al. (2021) [87] presented an inter-cascade GAN to segment the left atrium and atrial scars in an end-to-end way. The application of GAN-based methods to achieve automatic segmentation of cardiac regions solves the practical problems in the field of cardiac medicine to a certain extent.

3.2. 5. Abdomen

Deep neural networks have been widely used to automate organ segmentation on abdominal CT scans. **Table 7** summarizes the GAN-based segmentation methods and the similarities and differences of

Table 8

Segmentation GAN-based methods – Pelvic. List of abbreviations: VOE = volumetric overlap error; SMBD = symmetric mean boundary distance.

Paper	Region	Modality	Method	Loss	Data	Performance
Kohl et al. (2017) [100]	Tumor lesion, surrounding area and metastatic area	MRI	FCN GAN	Adv	Unknown Train: 76 Test: 38 Validation: 38	DSC = 0.41 ± 0.28 Sen = 0.55 ± 0.36
Jia et al. (2019) [101]	Prostate gland	MRI	3D APA-Net (3D adversarial pyramid anisotropic convolutional deep neural network)	3D cross entropy, binary cross entropy	PROMISE12 Train: 50, 30 ASPS13 Train: 60 Test: 10 HYBRID unknown	(whole, base, apex) DSC = 0.906, 0.891, 0.869 ABD = 1.454, 1.629, 1.532 DSC = 0.893 (±0.025) ABD = 1.167 (±0.285) DSC = 0.901 (±0.033) ABD = 0.944 (±0.364)
Wang et al. (2021) [102]	Prostate	MRI	U-Net GAN	Adv, mean absolute error loss, dice loss	Unknown, Decathlon, NCI-ISBI 2013, QIN-PROSTATE-Repeatability, PROMISE12 Train: 355 Test: 70	(Experiment data, Promise 12) ASD = 0.51 ± 0.30, 1.02 ± 0.83 VOE = 15.28 ± 4.61, 23.60 ± 0.10 HD = 11.58 ± 6.73, 7.57 ± 3.72 DSC = 0.9166 ± 0.0280, 0.8624 ± 0.0709
Kan et al. (2021) [103]	Prostate, uterus	CT	U-Net CGAN Pix2Pix	Adv, binary cross entropy loss, L ₁ loss	Unknown Train: Unknown Test: Unknown	(prostate, uterus) DSC = 0.929 ± 0.200, 0.724 ± 0.0413 HD = 0.338 ± 0.905, 0.709 ± 1.56
Sultana et al. (2020) [104]	Prostate, bladder and rectum	CT	FCN GAN U-Net	Adv, weighted dice, Least squared generator	Unknown Train: 100 Test: 15	(prostate, bladder, rectum) DSC = 0.90 ± 0.05, 0.96 ± 0.06, 0.91 ± 0.09 HD = 5.21 ± 1.17, 4.37 ± 0.56, 6.11 ± 1.47
Brion et al. (2021) [105]	Bladder, rectum, and prostate	CT CBCT	U-Net GAN	Adv, dice loss, cross-entropy loss	Unknown Train: 60 Test: Unknown	(bladder, rectum, and prostate) DSC = 0.868 ± 0.094, 0.762 ± 0.093, 0.719 ± 0.083 SMBD = 2.90 ± 2.09, 2.96 ± 1.23, 3.66 ± 1.36
Zhang et al. (2021) [106]	Prostate, bladder, rectum, left femur, and right femur	CT	U-Net GAN	Binary cross entropy loss, multi-class cross-entropy loss	Unknown Train: 90 Validation: 10 Test: 20	(prostate, bladder, rectum, left femur, and right femur) DSC = 0.88 ± 0.11, 0.97 ± 0.07, 0.86 ± 0.12, 0.97 ± 0.01, 0.97 ± 0.01 average HD = 1.58 ± 1.77, 1.91 ± 1.29, 3.14 ± 2.39, 1.76 ± 1.57, 1.92 ± 1.01 average HSD = 2.11 ± 2.03, 2.36 ± 2.43, 3.05 ± 2.11, 1.99 ± 1.66, 2.00 ± 2.07
Lei et al. (2021) [107]	Bladder, prostate, rectum, left and right femoral heads	CT MRI	CycleGAN	Adv, dice loss	Unknown Train: 64 Test: 16	(bladder, prostate, rectum, left femoral head, right femoral head) DSC = 0.93 ± 0.09, 0.88 ± 0.06, 0.88 ± 0.05, 0.94 ± 0.05, 0.94 ± 0.04 95% percentile HD = 4.84 ± 4.57, 5.49 ± 3.39, 7.04 ± 9.10, 5.25 ± 6.47, 5.28 ± 6.70 MSSD = 1.43 ± 1.10, 1.55 ± 0.97, 1.86 ± 1.33, 1.29 ± 1.07, 1.24 ± 0.96 RMSD = 2.27 ± 1.95, 2.46 ± 1.38, 3.08 ± 3.05, 2.16 ± 2.18, 2.16 ± 2.21

abdomen anatomical regions.

In abdominal scan images, the spatial boundaries of adjacent organs are difficult to identify, and the relative sizes of different target organs vary greatly, making it difficult for traditional deep learning methods to accurately segment each organ. Yang et al. (2017) [89] and Kim and Ye (2018) [90] used GAN for liver segmentation, which effectively improves the segmentation accuracy and processing speed. Huo et al. (2018) [91] [92] first proposed a splenomegaly segmentation network based on CGAN, and then they proposed an end-to-end synthesis and segmentation network to achieve accurate segmentation of the spleen. Liu et al. (2019) [93] used GAN to conduct label assignment and output probabilistic maps, thus realizing accurate segmentation of colorectal tumors. Poorneshwaran et al. (2019) [94] presented a colon polyp region segmentation method with an improved pix2pix framework. Ruan

et al. (2020) [95] added a multi-scale feature extractor and a locator of the area of interest to GAN to achieve fast and accurate kidney tumor segmentation. Huang et al. (2021) [96] and Li et al. (2021) [97] segmented the stomach and pancreas using different adversarial networks. Besides, Sandfort et al. (2019) [98] and Conze et al. (2021) [99] used GAN to achieve automatic multi-organ segmentation of abdominal CT and MR images, achieving effective simultaneous segmentation of multiple organs.

3.2. 6. Pelvic

The complex pelvic structure of the human body has great variability, which brings about various clinical problems, such as variable shape, high similarity of signals of different structures, and lack of annotated data. Automatic segmentation and modeling of pelvic structure

Table 9

Segmentation GAN-based methods – Spine.

Paper	Region	Modality	Method	Loss	Data	Performance
Han et al. (2018) [108]	Spine	MRI	Spine-GAN (Recurrent GAN)	Adv, Binary classification loss, Multi-class Cross-entropy,	Unknown Train: 253 Test: unknown	High PA = 0.962 DSC = 0.871 Sen = 0.891 Spe = 0.860
Sekuboyina et al. (2018) [109]	Vertebrae	CT (3D)	Btrfly Net (Butterfly-shaped network)	Adv, Btrfly-Net	Unknown Train: 242 Test: 60	Pre = 0.84 Rec = 0.83 F_1 -score = 0.84
Liu. (2019) [110]	Femur, femur cartilage, tibia, tibia cartilage	MRI	CycleGAN	Adv, Cycle consistency	T2-FSE Train: 60 Test: unknown PD-FSE Train: 60 Test: unknown	(Femur bone, Tibia bone, Femoral cartilage, Tibial cartilage) DSC = 0.97 ± 0.01, 0.95 ± 0.00, 0.66 ± 0.03, 0.65 ± 0.06 DSC = 0.95 ± 0.01, 0.93 ± 0.02, 0.81 ± 0.02, 0.75 ± 0.06
Gaj et al. (2020) [111]	Knee cartilage, meniscus cartilage Chambers (FC, LTC, MTC and PC) and meniscus (LM and MM)	3D DESS MRI	U-Net CGAN	Adv, Segmentation, Feature matching	Osteoarthritis Initiative Train: 62 Test: 8 Validation: 18	(FC, LTC, MTC, PC, LM, MM, Average) DSC = 0.8972 ± 0.023, 0.9181 ± 0.013, 0.8609 ± 0.038, 0.8417 ± 0.058, 0.8950 ± 0.023, 0.8738 ± 0.045, 0.8811
Kessler et al. (2020) [112]	Femoral, tibial and patellar bone and cartilage, cruciate ligaments and muscle tissues	MRI	CGAN U-Net pix2pix	Adv, L_1	SKI10, OAI ZIB, AMROA Train: 70, 355, 8 Test: 30, 152, 2	(F Bone, T Bone, P Bone, F Cartilage, T Cartilage, P Cartilage, VM Muscle, GM Muscle, ACL, PCL) DSC = 0.968 ± 0.006, 0.950 ± 0.015, 0.936 ± 0.003, 0.875 ± 0.021, 0.810 ± 0.036, 0.863 ± 0.043, 0.914 ± 0.001, 0.837 ± 0.146, 0.652 ± 0.094, 0.374 ± 0.341
Wei et al. (2020) [113]	Femur, femoral head	X-ray	DCGAN	Adv, Dice	Unknown Train: 50 Test: 30	(femur, femoral head) DSC = 0.9762, 0.9786 Pre = 0.9549, 0.9854 Rec = 0.9622, 0.9841 F -score = 0.9585, 0.9847
Alsinan et al. (2020) [114]	Bone shadow	Ultrasound	CGAN	Adv, Cross-entropy loss,	Unknown Train: 27 Test: unknown	(Dataset I, Dataset II) IOU = 0.9277, 0.9023 DSC = 0.9603, 0.9354 Rand error = 0.4841, 0.5990 Hamming loss = 0.0873, 0.0976
Gong et al. (2021) [115]	Discs, neural foramens, thecal sacs, and posterior arches	MRI	GAN GCN	Sigmoid cross-entropy loss, softmax cross-entropy loss	Unknown Train: 119 Test: 50	DSC = 0.949 ± 0.018 Acc = 0.939 ± 0.026 ASSD = 0.127 ± 0.064 Sen = 0.954 ± 0.022 Spe = 0.912 ± 0.028 F -score = 0.953 ± 0.022

have much significance to doctors' clinical work. Table 8 summarizes the GAN-based segmentation methods and the similarities and differences of pelvic anatomical regions.

Accurate segmentation of the prostate and surrounding organs at risk is essential to prostate radiation planning. Kohl et al. (2017) [100], Jia et al. (2019) [101], and Wang et al. (2021) [102] used GAN to segment the prostate, a reproductive organ unique to males in the pelvic cavity. Meanwhile, Kan et al. (2021) [103] added a built-in auxiliary classifier into GAN to segment the prostate and the female reproductive organ, i.e., uterus. Sultana et al. performed simultaneous segmentation of multiple organs in the pelvic cavity [104–107]. Among them, Sultana et al. (2020) [104] used a multi-class 3D U-net to perform coarse segmentation of the pelvic structure, and then they used improved GAN to perform fine segmentation of the organs. Lei et al. (2021) [107] used dual pyramid networks for feature extraction and CycleGAN to generate synthetic MRI to provide supplementary information for simultaneous segmentation of multiple organs. These methods effectively improve the segmentation accuracy of multiple organs.

3.2. 7. Spine

The segmentation of bone images is faced with a few challenges, such as low signal-to-noise ratio, imaging artifacts, and bone surfaces with a thickness of a few millimeters. To overcome these limitations, various bone segmentation and registration methods have been proposed. Table 9 summarizes the GAN-based segmentation methods and the similarities and differences of spine anatomical regions.

Han et al. (2018) [108] and Sekuboyina et al. (2018) [109] used GAN to segment the spine. The difference between the two methods is that Han et al. segment the synchronized semantics of more than 160 spinal structures, while Sekuboyina et al. segment the local spine. Liu et al. combined GAN with different neural networks to segment the knee joint in MRI images [110–112].

In addition, Wei et al. (2020) [113] proposed an improved DCGAN to segment the femoral region, which helps to evaluate the femoral neck-shaft angle according to the segmentation results. Alsinan et al. (2020) [114] improved CGAN and realized real-time segmentation of bone shadow on ultrasound images; Gong et al. (2021) [115] used GAN to achieve simultaneous segmentation and disease diagnosis of discs, neural foramens, thecal sacs, and posterior arches on axial MRI images.

3.2. 8. Multiple organ

In multi-organ segmentation, the target organ of different patients usually varies greatly in shape and position. Meanwhile, the contrast of contour in the image is relatively low, and the spatial boundary of adjacent organs is difficult to determine, which makes it difficult to segment and label the organs. The segmentation methods based on deep learning can segment the organs at risk on different types of images, thus improving the efficiency of manual depiction in clinical treatment and reducing anatomical errors. Table 10 summarizes the GAN-based segmentation methods and the similarities and differences of multiple organ anatomical regions.

Zhang et al. investigated the segmentation of organs at different parts

Table 10

Segmentation GAN-based methods - Multiple organ.

Paper	Region	Modality	Method	Loss	Data	Performance
Zhang et al. (2018) [116]	Lungs, heart, liver, bones	CT(3D)	TD-GAN	Binary cross entropies, Segmentation driven	Unknown Train: 968 Test: unknown	(Bone, Heart, Liver, Lung, mean) DSC = 0.835, 0.870, 0.817, 0.894, 0.854
Tong et al. (2019) [117]	Head and neck	CT MRI	SC-GAN (Shape constraint GAN)	Adv, Dice coefficient, Binary cross-entropy	PDDCA Train: 32 Test: unknown Unknown Train: 25 Test: unknown	(brainstem, optical chiasm, mandible, optical nerves, larynx, pharynx, parotid glands) DSC = 0.916, 0.589, 0.816, 0.703, 0.799, 0.706, 0.845 (brainstem, larynx) ASSD = 0.68, 1.70
Cai et al. (2019) [118]	Cardiovascular, pancreatic, mammogram	MRI CT X-ray	PatchGAN CycleGAN U-Net	Adv, cycle consistency loss, shape-consistency loss	Cardiac: Unknown (MRI, CT) Train: 71,2177 Test: 71,2177 Pancreatic: Unknown Train: 40 Test: 120 Mammogram: BCDR, INBreast Train: 58 Test: 58	Cardiac (CT, MRI) DSC = 0.744, 0.732 Pancreatic (CT, MRI) DSC = 0.788, 0.704 Mammogram (BCDR, INBreast) DSC = 0.750, 0.811
Pang et al. (2020) [119]	Lung, kidney and liver tumors	CT	CTumorGAN	MAE, MSE, Cross entropy, Dice	TCIA Train: 422 Test: unknown KITS2019 Train: 210 Test: unknown Unknown Train: 131 Test: unknown	Pre = 0.8662 DSC = 0.8388 JI = 0.7716 Spe = 0.9993 F ₁ -score = 0.8559 Rec = 0.8459
Yuan et al. (2020) [120]	Abdomen (liver, right kidney, left kidney, spleen), Brain	MRI	U-Net GAN	Adv, Dice, Classification, Cycle consistency, Cross-entropy	CHAOS2019 Train: 16 Test: 8 Medical Segmentation Decathlon Train: 80 Test: 20	(liver, right kidney, left kidney, spleen) DSC = 0.8820 ± 0.0586, 0.8396 ± 0.0849, 0.8348 ± 0.1146, 0.8047 ± 0.1030 ASSD = 5.40 ± 3.63, 3.25 ± 2.28, 4.82 ± 5.95, 9.46 ± 8.83 MSSD = 50.47 ± 14.37, 28.31 ± 17.95, 33.75 ± 29.73, 43.86 ± 18.45 (T1w, T1gd, T2w, FLAIR) DSC = 0.4471, 0.5974, 0.5, 0.41, 0.4851 HD = 13.37, 11.57, 12.70, 12.78 Sen = 0.4676, 0.6251, 0.5124, 0.5083 Spe = 0.9985, 0.9989, 0.9988, 0.9987
Wang et al. (2020) [121]	Optic disc, Fetal head, Lung, Liver	Ultrasound Fungus X-Ray CT	CycleGAN U-Net	Dice loss, cycle consistency loss, Adv, L ₂	DRIONS-DB and Drishti-gs, HC18, JSRT, CHAOS Train: 148, 702, 96, 14 Test: 42, 198, 28, 4 Validation: 21, 99, 14, 2	(Optic disc, fetal head, lung, liver) DSC = 0.961 ± 0.018, 0.962 ± 0.026, 0.926 ± 0.025, 0.933 ± 0.031 ASSD = 1.872 ± 1.224, 3.155 ± 2.153, 3.693 ± 1.178, 3.151 ± 1.071
Liu et al. (2021) [122]	Optic cup (OC), optic disc (OD), gray matter (GM), white matter (WM)	OCT MRI	GAN	Adv, dice loss, common cross-entropy loss	REFUGE, Drishti-GS, SCGM 2017 Segmentation Challenge 2017 Train: Unknown Test: Unknown	(REFUGE, Drishti-GS, SCGM 2017) REFUGE (OC, OD) Acc = 0.953, 0.894 DSC = 0.959, 0.926 HD = 7.2, 7.6 Drishti-GS (OC, OD) Acc = 0.961, 0.859 SCGM 2017(GM, WM) Acc = 0.843, 0.911 DSC = 0.723, 0.879 HD = 9.6, 7.8
Dai et al. (2021) [123]	Brain stem, left/right cochlea, left/right eye, larynx, left/right lens, mandible, optic chiasm, left/right optic nerve, oral cavity, left/right parotid, pharynx, and spinal cord	CBCT MRI CT	CycleGAN Feature pyramid network (FPN)	Binary cross entropy loss, dice loss	Unknown Train: 35 Test: 30	DSC = 0.87 ± 0.03, 0.79 ± 0.10/0.79 ± 0.11, 0.89 ± 0.08/0.89 ± 0.07, 0.90 ± 0.08, 0.75 ± 0.06/0.77 ± 0.06, 0.86 ± 0.13, 0.66 ± 0.14, 0.78 ± 0.05/0.77 ± 0.04, 0.96 ± 0.04, 0.89 ± 0.04/0.89 ± 0.04, 0.83 ± 0.02, 0.84 ± 0.07
Chen et al. (2021) [124]	Craniomaxillofacial bony structures and cardiac substructures	MRI CT	GAN	Adv, self-reconstruction loss, cross-reconstruction feature consistency losses	CQ500, ADNI Train: 50 Test: 8 MMWHS Challenge 2017 Train: 16 Test: 4	craniomaxillofacial bony structures DSC = 0.8100 ± 0.0136 ASSD = 1.35 ± 0.12 cardiac substructures DSC = 0.751 ± 0.98 ASSD = 5.5 ± 2.2

Table 11

Segmentation GAN-based methods - Microscopic image. List of abbreviations: ARI = adjusted rand index; AP = Area overlap; AD = Area difference; RSD = Symmetric RMS contour distance.

Paper	Region	Modality	Method	Loss	Data	Performance
Sadanandan et al. (2017) [125]	Spheres of different sizes, shapes, and light conditions	Cell (2D)	U-Net GAN	Weighted spatial cross entropy, Adv	Unknown Train: 3076 Test: unknown	F-score = 0.70 Pre = 0.74 Rec = 0.69
Zhang et al. (2017) [126]	Glandular, 3D fungus	Fungus 3D	DCAN VGG16	Adv, Multi-class cross-entropy, Binary-class cross-entropy	2015 MICCAI Gland Challenge Train: 85 Test: 20 Unknown Train: 4	F-score = 0.88 DSC = 0.865 HD = 74.55 Rec = 0.9302 Pre = 0.9428
Arbelle and Raviv (2018) [127]	Cells	Cell (2D)	GAN	Adv	H1299 Train: 72	F ₁ - Score = 0.9364 F-score = 0.858 Pre = 0.899 Rec = 0.82
Majurski et al. (2019) [128]	Retinal pigment epithelial stem cells	Cell (2D)	U-Net GAN	Adv, Cross entropy,	URL Train: 500 Test: 500	DSC = 0.611 ± 0.075 ARI = 0.151 ± 0.105
Mahmood et al. (2019) [129]	Multiple organ nuclei	Cell (2D)	CGAN	Adv, Cycle consistency, Binary cross entropy	Unknown Train: 34	J _I = 0.721 HD = 4.291 F ₁ -Score = 0.866
Gadermayr et al. (2019) [130]	Kidney histology proof	Cell (2D)	CycleGAN	Adv, cycle consistency loss	Unknown Train: 29 Test: 12	Unknown
Guo et al. (2019) [131]	Cells	Confocal images Light sheet images	U-Net GAN	Adv, cross entropy loss	Unknown Train: 4	DSC = 0.709
de Bel et al. (2021) [132]	Colon tissue and kidney tissue	Cell (2D)	CycleGAN U-Net PatchGAN	Adv, Cycle consistency, L ₁	Unknown (colon, kidney) Train: 26, 41	(colon, kidney) DSC = 0.66, 0.85
Liu et al. (2021) [133]	Eyes diseases	Cell (2D)	CGAN U-Net PatchGAN	Adv, L ₁ , partial intensity	Unknown Train: 248	DSC = 0.89 ± 0.07 AP = 0.81 ± 0.01 AD = 0.16 ± 0.18 ASSD = 1.2 ± 0.9 RSD = 1.5 ± 1.1 MSSD = 2.9 ± 2.5
Yang et al. (2021) [134]	Corneal nerve fiber	Microscopy	U-Net GAN	Adv, dice loss	Unknown Train: Unknown Test: Unknown	DSC = 0.8921 ± 0.0016, 0.8908 ± 0.0016, 0.8762 ± 0.0018 IOU = 0.8077 ± 0.0042, 0.8053 ± 0.0038, 0.7822 ± 0.0046 Sen = 0.8840 ± 0.0024, 0.8812 ± 0.0036, 0.8679 ± 0.0029 AUC = 0.9372 ± 0.0006, 0.9355 ± 0.0008, 0.9297 ± 0.0007

in different imaging modes [116–124]. Zhang et al. (2018) [116] proposed TD-GAN (Task Driven GAN) to segment multiple organs on X-ray images in an unsupervised way for the first time. Tong et al. (2019) [117] added shape constraints to GAN and used a deep supervised fully convolutional DenseNet as a segmentation network to segment multiple organs in the head and neck. Based on [20], Yuan et al. (2020) [120] broke the limitation of 2D segmentation and realized 3D image segmentation of abdominal organs and brain tumors. Chen et al. (2021) [124] introduced a diverse data augmentation GAN to train a segmentation model for an unannotated target image domain by borrowing the information from an annotated source image domain. Compared with the single-organ segmentation method, the multi-organ segmentation method is generally more robust and universal, but the accuracy is limited.

3.2. 9. Microscopic image

Microscopic processing is an important research field in medical and biological image processing. Due to the complexity of microscopic image content and the lack of obvious distinction between the target and the background, automatic segmentation is challenging. Table 11 summarizes the GAN-based segmentation methods and the similarities and differences of microscopic image anatomical regions.

Currently, different GANs have been employed to segment microscopic images [125–134]. For instance, Sadanandan et al. (2017) [125]

performed feature extraction on different scales and improved adversarial loss to obtain more stable results of spheroids image segmentation. Mahmood et al. (2019) [129] first generated an annotated multi-organ nuclei image dataset through an unpaired GAN model, and then they performed image segmentation by using a context-aware adversarial network. de Bel et al. (2021) [132] improved the regular CycleGAN by adding residual learning. Then, they adopted the improved network to reduce the variation between strains in histopathology. Liu et al. (2021) [133] combined a statistical model with CGAN to efficiently generate high-quality annotated images to aid in cell segmentation.

3.2. 10. Others

In addition to the above segmentation areas, GAN can also be used for segmenting various tissue and organs, such as skin lesions and cell lymphoma. Table 12 summarizes the GAN-based segmentation methods and the similarities and differences of other anatomical regions.

Izadi et al. (2018) [135], Xue et al. (2018) [136], and Lei et al. (2020) [137] segmented skin lesions with improved GAN. Hu et al. (2020) [138] divided the segmentation of extranodal natural killer/T cell lymphoma into two stages: coarse segmentation and fine segmentation. Wang et al. (2020) [139] added the structure of U-net to GAN to improve the segmentation of esophagus on OCT images. Gadermayr et al. (2019) [140] segmented the muscle tissue on MRI images by GAN, while Nishiyama et al. (2021) [141] used CGAN to perform accurate

Table 12

Segmentation GAN-based methods – Others.

Paper	Region	Modality	Method	Loss	Data	Performance
Izadi et al. (2018) [135]	Skin lesions	Dermoscopic images	U-Net GAN	Adv, Binary cross-entropy	DermoFit Train: 1040 Test: 260	DSC = 0.898 JI = 0.812 Sen = 0.891 Spe = 0.971 Acc = 0.942
Xue et al. (2018) [136]	Skin lesions	Dermoscopic images	SegAN (End-to-end GAN)	Adv, Multi-scale L ₁	ISIC 2017 Train: 2000 Test: 600	Acc = 0.941 JI = 0.785 DSC = 0.867
Lei et al. (2020) [137]	Skin lesions	Dermoscopic images	UNet-SCDC GAN (Skip connection and dense convolution GAN)	Adv, Conditional discriminative	ISIC 2016 (2016, 2017, 2018) Train: 900 Test: 379 ISIC 2017 Train: 2000 Test: 600 ISIC 2018 Train: 2296 Test: 300	Acc = 0.960, 0.935, 0.929 Sen = 0.937, 0.835, 0.953 Spe = 0.968, 0.976, 0.911 JI = 0.871, 0.771, 0.824 DSC = 0.931, 0.859, 0.885
Hu et al. (2020) [138]	Extranodal natural killer/T cell lymphoma	¹⁸ F-FDG PET/CT	U-Net GAN	Adv, Multi-scale L ₁	Unknown Train: 74 Test: 9	DSC = 0.7115 ± 0.132 Sen = 0.7472 ± 0.185 HD = 5.9781 ± 9.317 AVD = 0.3711 ± 0.421
Wang et al. (2020) [139]	Guinea pig's esophagus	OCT	U-Net GAN	Adv, Multi-class cross-entropy, L ₁ , Dice	Unknown Train: 4 Test: 2	pixel-wise accuracy = 0.9717 ± 0.0256 DSC = 0.9533 ± 0.0218 ASSD = 4.57 ± 1.99 HD = 28.82 ± 8.24
Gadermayr et al. (2019) [140]	Muscle tissue	MRI	CycleGAN ResNet	Adv, cycle consistency loss	Unknown Train: 25 Test: 16	(moderately affected subjects, severe fatty infiltrations) DSC = 0.91, 0.88
Nishiyama et al. (2021) [141]	Gluteus medius	CT	CGAN pix2pix	L ₁ , Adv	Unknown Train: 7 Test: 1	DSC = 0.748 Volume similarity = 0.247 shape similarity = 1.394

gluteus medius volume evaluation.

Table A1–10 in the appendix summarizes the additional information of the above studies. In these studies, different loss functions and optimizers were used for training with dozens to more than a thousand images. These GAN-based segmentation methods adopted three different learning styles, including supervision, semi-supervision, and unsupervision. Meanwhile, they exploited Dice similarity coefficient and other evaluation indexes to evaluate the corresponding results. However, there are some limitations in this review, and it is difficult to clearly judge the methods proposed in the above literature.

4. Discussion

Since GAN was introduced into the field of deep learning in 2014, it has received extensive attention from academia and industry, and its popularity has grown rapidly. Currently, a plethora of high-quality papers have been published and discussed, and many companies engaged in artificial intelligence research are making a lot of effort to develop and promote GAN models. Our review finds that the application of GAN in the field of medical image segmentation emerged in 2016. In recent years, because of the advantages of GAN, such as less demand for training data, good generation effect, and easy combination with other neural networks, the segmentation methods based on GAN have been increasingly applied in medical image research.

In Section 2, the principles of GAN and some of its extension models are briefly introduced, and the usage scenarios of different extension models are compared. As for the generative model G , its parameter update is not optimization of the likelihood of data but a back-propagation gradient from the discriminant model D . Also, GAN can avoid the Markov chain learning mechanism, which makes it different from the traditional probabilistic generation model. Besides, GANs conduct sampling and inference directly, so the application efficiency of GAN is improved, and the practical application scenarios of GAN are more extensive.

In Section 3, the application of GAN in the field of medical image segmentation is summarized. As a flexible design framework, the GAN-based deep learning models have made great contributions to improving the accuracy of medical image segmentation. According to the summary in the third part, these models are mainly improved from the following two aspects. (1) Increase or improve the loss function. Due to the flexibility of GAN, various kinds of loss functions can be integrated into the GAN model. Therefore, the performance of the model can be effectively improved by designing different types of loss functions for different tasks. (2) Combine GAN with other neural networks [142–145]. GAN's generation model and discriminant model can be parameterized by any differentiable function. This unique learning mode enables GAN to extract semantic segmentation features more effectively and improve the performance of network segmentation.

Meanwhile, in the process of studying the application of GAN in medical image segmentation, the application of GAN in other medical image processing fields was also found. For example, the coronavirus disease (COVID-19), which has been recognized as a pandemic by the World Health Organization, has spread rapidly since December 2019. Goel et al. used GAN and related models to provide assistance for automatic detection of the virus, which has much significance for preventing the further spread of the infectious disease [146–152]. Besides, GAN also has many interesting applications in other medical image processing fields such as medical image synthesis, medical image enhancement, and medical image reconstruction ([3,4]). These efforts will also effectively reduce the burden of clinicians and facilitate the development of the medical imaging field.

Although GAN's new progress has provided new ideas for medical image segmentation, it still has some limitations in practice. On the one hand, the research of GAN in the field of medical image segmentation is mainly technology-oriented, and the evaluation indexes adopted are also those in the field of computers. The vast majority of the studies discussed in this review evaluated the possibility of implementing the model rather than the effectiveness of GAN-based methods in practical

clinical applications. For any medical application, it is expected to validate the technology in accordance with medical rules. On the other hand, GAN, as a generative model, has a few problems such as non-convergence, difficulty in training, mode collapse, and mode jump. Secondly, when the training results of GAN are applied to a new application, the model needs transfer learning to maintain performance, which undoubtedly leads to the low repeatability of clinical applications. Besides, the interpretability of GAN is very poor. It's just a black-box mapping function, in which the input is a random variable, and the output is a desired distribution of the data. This is the main obstacle to its practical application in the medical field. Therefore, researchers should pay attention to overcome the instability, low repeatability, and uninterpretability of GAN.

Moreover, it is challenging to obtain the recognition of clinicians and patients for the data quality generated by GAN. As Mazurowski et al. pointed out in Ref. [153], the clinical use of artificial intelligence in radiology is still debated. When GAN is used in clinical settings, the biggest risk is that it may generate false information. In the process of data generation, some disease information that does not exist may be inadvertently generated; also, some disease information that does exist may also be ignored as irrelevant information. Therefore, the use of GAN in clinical practice should be cautious. Similar to other applications, the GAN-based applications should be well validated [154]. In the short term, the segmentation results generated by GAN-based methods should still be reviewed by experienced clinicians, and the results that rely on GAN auto-segmentation should be performed only within a limited experimental range. In addition, the same as other deep learning

methods, ethical and legal issues need to be considered when GAN is used in the clinic [155]. Although GAN has some limitations, if it can be used reasonably and carefully, it will bring many new possibilities for medical image segmentation.

In conclusion, GAN has a broad application prospect in medical image processing. Various GAN-based methods and their variants have attracted much attention, which effectively promotes the application and development of deep learning algorithms in medical image processing. However, obtaining the recognition of these methods by clinicians and patients is still a huge challenge. Besides, GAN also has some limitations, such as instability, low repeatability, and uninterpretability. The solution to these problems will provide a new way and direction for the development of GAN.

Declaration of competing interest

The authors declare that they have no known competing financial interests or personal relationships that could have appeared to influence the work reported in this paper.

Acknowledgment

This work was supported by the National Natural Science Foundation of China [61971271]; the Taishan Scholars Project of Shandong Province [Tsqn20161023]; and the Primary Research and Development Plan of Shandong Province [No. 2018GGX101018, No. 2019QYTPY020].

Appendix

Table A.1

Segmentation GAN-based methods – Brain.

Paper	DOI	Optimizer	Hyper-parameter	Training configuration	Data url	Code	Algorithm url
Li et al. (2017) [17]	10.1007/978-3-319-75238-9_11	Adam	beta ₁ = 0.9, beta ₂ = 0.999 Epsilon = 1e ⁻⁸ Learning rate = 0.001, 0.0001 Batch size = 128, 256	Unknown	https://www.med.upenn.edu/sbia/brats2017/data.html	No	Unknown
Rezaei et al. (2017) [18]	10.1007/978-3-319-75238-9_21	Unknown	Unknown	Task1 : parallel Pascal Titan X GPUs, five days Task2 : single Pascal Titan X GPU, 12 h	https://www.med.upenn.edu/sbia/brats2017/data.html	No	Unknown
Xue et al. (2018) [19]	10.1007/s12021-018-9377-x	RMSProp	Learning rate = 0.00002 Batch size = 64	Unknown	https://www.smir.ch/BRATS/Start2013 https://www.smir.ch/BRATS/Start2015	No	Unknown
Yuan et al. (2019) [20]	10.1007/978-3-030-32248-9_26	Adam	Learning rate = 1e ⁻⁴ Batch size = 8 Epochs = 100	Intel i7 8700K CPU and an NVIDIA GTX 1080Ti GPU	Unknown	No	Unknown
Nema et al. (2020) [21]	10.1016/j.bspc.2019.101641	Unknown	Epochs = 200	NVIDIA DGX station with processor 2.2 GHz, Intel Xeon E5-2698, NVIDIA Tesla V100 4 × 16 GB GPU	https://www.smir.ch/BRATS/Start2015 https://www.med.upenn.edu/sbia/brats2017/data.html	No	Unknown
Li et al. (2020) [22]	10.1142/S0218001421570020	Adam	Batch size = 1 Learning rate = 5 × 10 ⁻⁴ λ = 0.2 Epochs = 100, 200	NVIDIA GTX 1080Ti GPU	https://www.med.upenn.edu/sbia/brats2017/data.html	No	Unknown
Conte et al. (2021) [23]	10.1148/radiol.2021203786	Adam	Epochs = 300 Batch size = 1 Learning rate = 0.0002 β ₁ = 0.5 β ₂ = 0.999	NVIDIA V100 card with 32 GB of memory	https://www.med.upenn.edu/sbia/brats2017/data.html	Yes	https://github.com/gemmeucci/pix2pixRAD
	10.1002/mp.14480	SGD				No	Unknown

(continued on next page)

Table A.1 (continued)

Paper	DOI	Optimizer	Hyper-parameter	Training configuration	Data url	Code	Algorithm url
Cheng et al. (2021) [24]			Momentum = 0.9 Weight decay = 0.0005 Learning rate = 0.005 Batch size = 1 Batch size = 300	NVIDIA GTX Titan X Graphics	https://www.med.upenn.edu/cbica/brats2019/data.html		
Moeskops et al. (2017) [25]	10.1007/978-3-319-67558-9_7	RMSprop	Learning rate = 0.001	Titan X Pascal GPU	http://www2.imm.dtu.dk/projects/BRATS2012/ https://mrbrains13.isi.uu.nl/	No	Unknown
Mondal et al. (2018) [26]	arXiv:1810.12241	Adam	Batch size = 30 Learning rate = 0.0001 Momentum = 0.5	Unknown	http://iseg2017.web.unc.edu/reference/h http://mrbrains13.isi.uu.nl	Yes	https://github.com/arnab39/FewShotGAN-Unet3D
Taek Oh et al. (2020) [27]	10.1007/s10278-020-00321-5	SGD Adam	Batch size = 1 Learning rate = 0.0002 $\beta_1 = 0.5 \beta_2 = 0.999$	NVIDIA Geforce GTX 1080 Ti GPU	http://adni.loni.usc.edu/	No	Unknown
Delisle et al. (2021) [28]	10.1016/j.media.2021.102191	Adam	Epoch = 120, 70 $\lambda = 1.5$ Weight decay = 0.001 Learning rate = 0.001, 0.0001	NVIDIA Tesla V100 32 GB GPU	http://iseg2017.web.unc.edu/reference/h http://mrbrains13.isi.uu.nl http://fcon_1000.projects.nitrc.org/indi/abide/	Yes	https://github.com/plde/lisdeepNormalize
Zhao et al. (2018) [29]	10.1007/978-3-030-00937-3_82	Adam	Learning rate = $1e^{-4}$ Momentum = 0.9	Unknown	http://adni.loni.usc.edu/	No	Unknown
Chen et al. (2019) [30]	10.1109/TMI.2019.2935409	Adam	Learning rate = 10^{-4} $KK_k = 3 \alpha = 1 \lambda_1 = 0.5$ $\lambda_2 = 0.05 \lambda_3 = 0.1$ $\lambda_4 = 0.5 \lambda_5 = 0.5$	Unknown	http://adni.loni.usc.edu/ http://headctstudy.cure.ai/dataset	No	Unknown
Shi et al. (2019) [31]	10.1186/s12938-019-0623-8	SGD	Batch size = 5 Learning rate = 10^{-5} Momentum = 0.99 Weight decay = 10^{-4}	Nvidia GPU	http://isip.bit.edu.cn/kyxz/xzlw/134492.htm	No	Unknown
Delannoy et al. (2020) [32]	10.1016/j.combiomed.2020.103755	Adam	Batch size = 32 $\lambda_{gp} = 100 \lambda_{adv} = 0.001$ Patch size = 643	Tesla P100 GPU and 2 Intel® Xeon™ Gold “Skylake” 6132 CPU	http://www.developingconnectome.org http://epipage2.inserm.fr	Yes	https://pypi.org/project/SegSRGAN https://github.com/koopa31/SegSRGAN
Li et al. (2021) [33]	10.1002/mp.15212	Unknown	Learning rate = 0.001 Momentum = 0.5 Batch size = 1	A standard workstation with one NVIDIA TITAN X GPU 12G is used for GPU calculation, one day	https://neobrain12.isi.uu.nl/?page_id=52 http://www.developingconnectome.org	Yes	https://github.com/lb-whu/RAS-NET/
Alex et al. (2017) [34]	10.1117/12.2254487	RMSProp	Unknown	Unknown	Unknown	No	Unknown
Kamnitsas et al. (2017) [35]	10.1007/978-3-319-59050-9_47	Unknown	Learning rate = 0.001 $\alpha_{max} = 0.05$	Titan X GPUs	Unknown	Yes	https://github.com/deepmedic/deepmedic
Kuang et al. (2020) [36]	10.1088/1361-6560/aba166	Adam	Unknown	Linux workstation with 2 T V100-PCIE-16GB GPUs	Unknown	Yes	https://github.com/WuChana/IschemicLesionSegmentationCT
Finck et al. (2020) [37]	10.1097/RLI.0000000000000640	Unknown	Unknown	NVIDIA Titan V, Santa Clara, CA, 12h	Unknown	Yes	https://github.com/hongweilibrain/DiamondGAN/
La Rosa et al. (2021) [38]	10.1016/j.combiomed.2021.104297	Adam	$\alpha = 150 \beta = 5$ Batch size = 1 Learning rate = $1e^{-5}$	NVIDIA Tesla P100 GPU	Unknown	Yes	https://github.com/FrancescoCoLR/synMP2RAGE

Table A.2

Segmentation GAN-based methods – Eye.

Paper	DOI	Optimizer	Hyper-parameter	Training configuration	Data url	Code	Algorithm url
Lahiri et al. (2017) [39]	10.1109/CVPRW.2017.110	Adam	Learning rate = 10^{-4} Decay factor = 0.8 Slope of leaky ReLU = 0.1	Unknown	https://drive.grand-challenge.org/	No	Unknown
Mahapatra et al. (2017) [40]	10.1007/978-3-319-66179-7_44	Adam	Iterations = 105 Learning rate = 10^{-3}	NVIDIA Tesla K40 GPU with 12 GB RAM	https://drive.grand-challenge.org/ https://cecas.clemson.edu/~ahoover/stare/ https://www.idiap.ch/software/bob/docs/bob/bob.db.chasedb1/master/index.html https://drive.grand-challenge.org/ https://cecas.clemson.edu/~ahoover/stare/ https://cremi.org/data/ http://www.aylward.org/news/isbi2013gr andchallenges	Yes	https://github.com/orobix/retina-unet
Javanmardi and Tasdizen (2018) [41]	10.1109/isbi.2018.8363637	Unknown	Unknown	Unknown	https://drive.grand-challenge.org/ https://cecas.clemson.edu/~ahoover/stare/ https://cremi.org/data/ http://www.aylward.org/news/isbi2013gr andchallenges	No	Unknown
Iqbal and Ali (2018) [42]	10.1007/s10916-018-1072-9	Adam	Learning rate = $2e^{-4}$ $\lambda = 10$	Standard PC with Intel Core i5 CPU and GeForce GTX 1080 GPU	https://drive.grand-challenge.org/ https://cecas.clemson.edu/~ahoover/stare/	No	Unknown
Son et al. (2019) [43]	10.1007/s10278-018-0126-3	Adam	Learning rate = $2e^{-4}$ $\beta_1 = 0.5 \beta_2 = 0.999$	Unknown	https://drive.grand-challenge.org/ https://cecas.clemson.edu/~ahoover/stare/	Yes	https://bitbucket.org/woaldnd/retinagan
Yang et al. (2020) [44]	10.1007/s10278-020-00339-9	Adam	$\lambda = 0.1$ Batch size = 1 Learning rate = $2e^{-4}$ Momentum = 0.5	Intel Core i7-8700 CPU with GeForce GTX 1060 GPU 10 h	https://drive.grand-challenge.org/ https://cecas.clemson.edu/~ahoover/stare/	No	Unknown
Schlegl et al. (2017) [45]	10.1007/978-3-319-59050-9_12	Adam	$\lambda = 0.1$	A Titan X graphics processing unit using CUDA 8.0	Unknown	No	Unknown
Jiang et al. (2019) [46]	10.1364/BOE.10.002355	Unknown	Unknown	Unknown	Unknown	No	Unknown
Schlegl et al. (2019) [47]	10.1016/j.media.2019.01.010	Adam RMSprop	Batch size = 64	Titan X graphics processing unit	Unknown	Yes	https://github.com/tSchlegl/f-AnoGAN
Wang et al. (2021) [48]	10.1364/BOE.426803	Unknown	Epoch = 40 Batch size = 2	Two NVIDIA 2080Ti GPUs	www.duke.edu/~sf59/Chiu_BOE_2014_dataset.htm https://doi.org/10.17632/rscbjr9sj.3	No	Unknown
Shankaranarayana et al. (2017) [49]	10.1007/978-3-319-67561-9_19	Unknown	Deviation = 0.02 Epochs = 200 Learning rate = 10^{-4}	Single Pascal Titan X GPU, 4 h	https://www.idiap.ch/software/bob/docs/bob/bob.db.rimoner3/stable/index.html	No	Unknown
Wang et al. (2019) [50]	10.1109/TMI.2019.2899910	Adam SGD	MobileNetV2 Learning rate = $1e^{-3}$ Epochs = 200 Batch size = 16 Discriminator Learning rate = $2.5e^{-5}$ Segmentation network Learning rate = $1e^{-5}$	A server with four Nvidia Titan Xp GPUs	https://ieeexplore.ieee.org/document/86867807 https://www.idiap.ch/software/bob/docs/bob/bob.db.rimoner3/stable/index.html https://refuge.grand-challenge.org/	Yes	https://emmaw8.github.io/pOSAL
Kadambi et al. (2020) [51]	10.1007/s11548-020-02144-9	Adam	Discriminator, Encoder Learning rate = $1e^{-6}$ Decoder, Pooling layer Learning rate = $1e^{-5}$ $\gamma = 0.01 \lambda = 0.2$	Intel® Core™ i7-6800K CPU @ 3.40GHz × 12 and NVIDIA GeForce® GTX 1080 Ti graphic card	https://refuge.grand-challenge.org/ https://ieeexplore.ieee.org/document/86867807	No	Unknown
Luo et al. (2021) [52]	10.1007/s11548-021-02373-6	Adam SGD	Learning rate = $1e^{-3}, 2.5e^{-3}$	NVIDIA RTX 2080Ti GPU	https://ieeexplore.ieee.org/document/9370570	Yes	

(continued on next page)

Table A.2 (continued)

Paper	DOI	Optimizer	Hyper-parameter	Training configuration	Data url	Code	Algorithm url
Liu et al. (2018) [53]	10.1109/ACCESS.2018.2889321	SGD Adam	Momentum = 0.9 Epoch = 300 Batch size = 12	A GTX970 GPU, 0.1 s per B-scan	t/6867807 https://www.idiap.ch/software/bob/docs/bob/bob.db.rimoner3/stable/index.html https://refuge.grand-challenge.org/ http://people.duke.edu/~sf59/Srinivasan_BOE_2014_dataset.htm	No	Unknown
Tennakoon et al. (2018) [54]	10.1109/isbi.2018.8363842	Adam	SGD Momentum = 0.9 Learning rate = 0.1 Adam Learning rate = 10^{-4} beta ₂ = 0.99	Unknown	https://retouch.grand-challenge.org/	Yes	https://github.com/RuwanT/retouch
Jiang et al. (2018) [55]	10.1007/978-3-030-00949-6_27	Unknown	Unknown	Unknown	Unknown	No	Unknown
OuYang et al. (2019) [56]	10.1364/BOE.10.005291	Adam	λ = 100 α = 10 Epochs = 100 Learning rate = 2×10^{-3} Batch size = 4	A NVIDIA Tesla V100 16 GB GPU	Unknown	No	Unknown
Yildiz et al. (2021) [57]	10.1167/tvst.10.6.33	Adam	Learning rate = 0.0002	A single NVIDIA Tesla V100 GPU card (approximately 0.2 image per second)	Unknown	No	Unknown

Table A.3

Segmentation GAN-based methods - Chest and breast.

Paper	DOI	Optimizer	Hyper-parameter	Training configuration	Data url	Code	Algorithm url
Zhu et al. (2016) [58]	arXiv:1612.05970	Adam	Learning rate = 0.003	Unknown	http://medicalresearch.inescporto.pt/breastresearch/index.php/Get_INbreast_Database http://www.eng.usf.edu/cvprg/Mammography/DDSM/BCRP/bcrp.html	No	Unknown
Shen et al. (2019) [59]	10.1016/j.cmpb.2019.105012	Adam	Batch size = 1 Iterations = 300 Learning rate = 0.0002 Momentum = 0.5	NVIDIA GeForce GTX 1080 Ti GPU	http://medicalresearch.inescporto.pt/breastresearch/index.php/Get_INbreast_Database	No	Unknown
Han et al. (2020) [60]	10.1016/j.cmpb.2019.105275	Adam	Learning rate = 10^{-2} Batch size = 10 Momentum = 0.5	A 2.40 GHz Intel Xeon E5-2630 CPU and an NVIDIA GeForce GTX 1080Ti GPU	Unknown	Yes	https://github.com/fiy2W/BUS-GAN
Xing et al. (2020) [61]	10.1109/TCBB.2020.2978470	Adam	Epochs = 1500 Batch size = 1 Learning rate = 0.0002	A NVIDIA GeForce GTX 1080Ti GPU and an Intel i7-7700 CPU	Unknown	No	Unknown
Ma et al. (2020) [62]	10.1088/1361-6560/ab7e7f	Adam	Learning rate = 0.0002	Unknown	Unknown	No	Unknown
Li et al. (2021) [63]	10.1002/mp.14671	Adam	$\beta_1 = 0.5$ $\beta_2 = 0.999$ Batch size = 8 Learning rate = 0.0001	Unknown	https://wiki.cancerimagingarchive.net/display/Public/CBIS-DDSM/#97542eefbc8e4234a95231cbcd86cb1d http://medicalresearch.inescporto.pt/breastresearch/index.php/Get_INbreast_Database	No	Unknown
Chen et al. (2018) [64]	10.1007/978-3-030-00919-9_17	Adam	Learning rate = 0.002	Nvidia Titan Xp GPU	https://data.montgomerycountymd.gov/ http://db.jsrt.or.jp/eng.php	No	Unknown
Tan et al. (2021) [65]	10.1016/j.compmedimag.2020.101817	Adam	Learning rate = 10^{-5} Momentum = 0.9 Weight decay = 0.0005	Unknown	https://wiki.cancerimagingarchive.net/display/Public/LIDC-IDRI https://pubmed.ncbi.nlm.nih.gov/24772218/	No	Unknown
	10.1007/s11548-021-02454-6	Adam		Unknown		No	Unknown

(continued on next page)

Table A.3 (continued)

Paper	DOI	Optimizer	Hyper-parameter	Training configuration	Data url	Code	Algorithm url
Stiehl et al. (2021) [66]			Learning rate = 0.0002 Momentum = 0.5	42 GPUs (1440 h of computing time)			
Jin et al. (2018) [67]	10.1007/978-3-030-00934-2_81	Adam	Learning rate = 0.0001 $\beta_1 = 0.5 \beta_2 = 0.999$	A Tesla K40 GPU	https://wiki.cancerimagingarchive.net/display/Public/LIDC-IDRI	No	Unknown
Jain et al. (2021) [68]	10.1016/j.combiomed.2021.104811	Unknown	Batch size = 1 $\beta_1 = 0.5 \beta_2 = 0.999$ Epoch = 50	Unknown	https://wiki.cancerimagingarchive.net/display/Public/LIDC-IDRI	No	Unknown
Dai et al. (2018) [69]	10.1007/978-3-030-00889-5_30	Adam	Learning rate = 0.0002	A Titan X GPU	https://data.montgomerycountymd.gov/ http://db.jsrt.or.jp/eng.php	No	Unknown
Trullo et al. (2019) [70]	10.1117/1.JMI.6.1.014001	Unknown	Unknown	Unknown	https://www.aapm.org/	No	Unknown
Dong et al. (2019) [71]	10.1002/mp.13458	Adam	2.5D network Batch sizes = 40 3D networks Batch sizes = 20	A Titan XP 12 GB GPU, 2 h for the first network and 3.5 h for the second and third networks	https://www.aapm.org/meetings/2017AM/	No	Unknown
Guo et al. (2020) [72]	10.1088/1361-6560/ab652b	SGD Adam	Learning rate = 0.005	Unknown	Unknown	No	Unknown

Table A.4

Segmentation GAN-based methods – Cardiology.

Paper	DOI	Optimizer	Hyper-parameter	Training configuration	Data url	Code	Algorithm url
Dou et al. (2018) [73]	10.24963/ijcai.2018/96	RMSProp	Learning rate = 3×10^{-4} Decay rate = 0.98 Weight clipping = 0.03	Unknown	https://zmiclab.github.io/projects/mmwhs/	No	Unknown
Rezaei et al. (2018) [74]	10.1007/978-3-662-56537-7_89	Unknown	Unknown	On parallel Pascal Titan X GPUs, takes around three days	http://segchd.csail.mit.edu/data.html	No	Unknown
Zhang et al. (2018) [75]	arXiv:1802.09655	Adam	Learning rate = $2e^{-4}$	Unknown	Unknown	No	Unknown
Joyce et al. (2018) [76]	Corpus ID: 13972499	Adam	Unknown	Titan XGPU	https://zmiclab.github.io/projects/mmwhs/	No	Unknown
Dong et al. (2018) [77]	10.1007/978-3-030-00937-3_71	SGD	Learning rate = 0.0002 Momentum = 0.5 Batch size = 1 $\alpha = 0.6 \beta = 0.4$	NVIDIA Titan X GPU	Unknown	No	Unknown
Chartsias et al. (2018) [78]	10.1007/978-3-030-00934-2_55	Unknown	Unknown	Titan XGPU	https://acdc.creatis.insa-lyon.fr/	Yes	https://github.com/agis85/spatial-factorisation
Liu et al. (2019) [79]	10.1016/j.compmedimag.2018.11.001	Adam	Epochs = 200 Batch size = 1 Learning rate = 0.0002 Decay rate = 0.5 $v = 5 \mu_1 = 1.5 \mu_2 = 0.5$ $\gamma = 0.5 \lambda_1 = 2 \lambda_2 = 5$ $T = 0.3$	Single Pascal Titan X GPU, 1 s A personal computer equipped with dual core Intel i5-4200U processor and 4 GB RAM, 15.2 ± 4.6 s	Unknown	No	Unknown
Upendra et al. (2019) [80]	10.1007/978-3-030-21949-9_45	Unknown	Learning rate = 0.0008 Batch size = 8 Decay = 0.5 Epochs = 50 beta = 0.5	NVIDIA	https://acdc.creatis.insa-lyon.fr/	No	Unknown

(continued on next page)

Table A.4 (continued)

Paper	DOI	Optimizer	Hyper-parameter	Training configuration	Data url	Code	Algorithm url
Xu et al. (2020) [81]	10.1016/j.media.2019.101568	Adam	Batch size = 6 Learning rate = 0.001 $\lambda_1 = 10 \lambda_2 = 0.5$ $\lambda_3 = 1$ $\lambda_4 = 10 T = 25$	An 8x NVIDIA P100	Unknown	No	Unknown
Decourt and Duong (2020) [82]	10.1016/j.compbioimed.2020.103884	Adam	Weight decay = 10^{-4} Learning rate = 2.5×10^{-4} $\lambda_{\text{adv}} = 0.1 \lambda_{\text{semi}} = 0.001$	Titan Xp	https://acdc.creatis.insa-lyon.fr/ https://data.yorkopenrepository.org/dataset	No	Unknown
Shi et al. (2020) [83]	10.1109/EMBC44109.2020.9175334	Unknown	Learning rate = 2×10^{-5}	NVIDIA GTX 1080Ti GPUs, 5 days	Unknown	No	Unknown
Cui et al. (2021) [84]	10.1016/j.compbioimed.2021.104726	Unknown	Learning rate = 0.00015 Batch size = 4	Unknown	https://zmiclab.github.io/projects/mmwhs/	No	Unknown
Wu et al. (2021) [85]	10.1016/j.media.2020.101891	Adam	Learning rate = 0.001	A graphics processing unit (GPU) server with Intel i9-9900k Central Processing Unit (CPU), 32 GB DDR4 Random Access Memory (RAM), Nvidia GeForce TITAN RTX (24 GB RAM)	https://zmiclab.github.io/projects/mmwhs/	No	Unknown
Yang et al. (2021) [86]	10.1109/JBHI.2020.3028463	Adam	Learning rate = 10^{-4} Drop-out rate = 0.1	Nvidia GTX 1080Ti	https://acdc.creatis.insa-lyon.fr/	No	Unknown
Chen et al. (2021) [87]	10.1109/JBHI.2021.3077469	Adam	Learning rate = 0.001, 0.0001	Nvidia RTX 8000 GPU (48 GB GPU memory)	Unknown	No	Unknown
Gilbert et al. (2021) [88]	10.1109/TMI.2021.3051806	Unknown	Epoch = 200	Unknown	https://www.creatis.insa-lyon.fr/Challenge/camus/databases.html http://millionsondataset.com/tasteprofile/	Yes	https://adgilbert.github.io/data-generation/

Table A.5

Segmentation GAN-based methods – Abdomen.

Paper	DOI	Optimizer	Hyper-parameter	Training configuration	Data url	Code	Algorithm url
Yang et al. (2017) [89]	10.1007/978-3-319-66179-7_58	Unknown	$\lambda = 0.01$ Iterations = 100 Discriminator $k_D = 10$ Batch size = 8 Generator $k_G = 1$ Batch size = 4 Unknown	NVIDIA TITAN X GPU and the Theano/Lasagne library	https://sliver07.grand-challenge.org/	No	Unknown
Kim and Ye (2018) [90]	Corpus ID: 52215245	Unknown		Unknown	https://competitions.codalab.org/competitions/17094	No	Unknown
Huo et al. (2018) [91]	10.1111/12.2293406	Adam	Learning rate = 0.00001	Titan X Pascal GPU	Unknown	No	Unknown
Huo et al. (2018) [92]	10.1109/isbi.2018.8363790	Adam	G_1, G_2 and S Learning rate = 0.0001 D_1, D_2 Learning rate = 0.0002	Unknown	Unknown	No	Unknown
Liu et al. (2019) [93]	10.1002/mp.13584	SGD	Momentum = 0.5 Learning rate = 10^{-5}	16 GB of memory and an NVIDIA GeForce GTX 1080 graphics card	Unknown	No	Unknown
Poorneshwaran et al. (2019) [94]	10.1109/EMBC.2019.8857958	Adam	Iterations = 250 Learning rate = 0.000099 Epochs = 250 Decay = 75 Momentum = 0.99	Unknown	https://polyp.grand-challenge.org/databases/	No	Unknown
Ruan et al. (2020) [95]	10.1016/j.media.2020.101721	RMSProp Adam	RMSProp algorithm : Learning rate $\lambda_1 = 0.01$ Adam algorithm:	A Titan X GPU	Unknown	No	Unknown

(continued on next page)

Table A.5 (continued)

Paper	DOI	Optimizer	Hyper-parameter	Training configuration	Data url	Code	Algorithm url
Huang et al. (2021) [96]	10.1155/2021/ 6679603	Adam	Learning rate $\lambda_2 = 0.001$ Learning rate = 0.01 Momentum = 0.9 Weight decay = 0.0001 Countermeasure network: Momentum = 0.5 Learning rate = 0.0001, 0.0004 Segmentation network Batch size = 4 Learning rate = 0.0001	4.0 GHz Intel Core i7- 4790k CPU	Unknown	No	Unknown
Li et al. (2021) [97]	10.1088/1361-6560/ ac155f	Adam	Batch size = 1 Learning rate = 0.0001 Momentum = 0.9, 0.99	An NVIDIA GeForce GTX 1080Ti graphics card with 11 GB of memory	https://wiki.cancerimagingarchive.net/display/Public/Pancreas-CT	No	Unknown
Sandfort et al. (2019) [98]	10.1038/s41598-019- 52737-x	Unknown	Batch size = 4	2xNVIDIA K80, for a total of 4 logical GPUs with 12 GB each	http://medicaldecathlon.com/ https://academictorrents.com/details/80ecfcabede760cdbdf63e38986501f7be4d49	No	Unknown
Conze et al. (2021) [99]	10.1016/j. artmed.2021.102109	Adam	Learning rate = 10^{-5} Epoch = 6, 20 Batch size = 3, 5	Nvidia GeForce GTX 1080 Ti GPU	https://doi.org/10.5281/zenodo.3362844	No	Unknown

Table A.6

Segmentation GAN-based methods – Pelvic.

Paper	DOI	Optimizer	Hyper-parameter	Training configuration	Data url	Code	Algorithm url
Kohl et al. (2017) [100]	arXiv:1702.08014	Adam	Learning rate = 10^{-5}	Unknown	Unknown	No	Unknown
Jia et al. (2019) [101]	10.1109/ TMI.2019.2928056	Adam	Learning rate = 10^{-4} betas = 0.9, 0.999 Weight decay = 10^{-6} $\lambda = 2.5$ Batch size = 16 Iteration = 10000	Linux two Intel(R) Xeon(R) E5- 2620 v4 2.10GHz $\times 8$ CPUs, 128 GB memory and four Nvidia Geforce GTX 1080Ti 11 GB GPUs PROMISE12, ASAP13 and hybrid databases Time = 10, 12 and 15 h	https://promise12.grand-challenge.org/ https://wiki.cancerimagingarchive.net/display/DOI/NCI-ISBI+2013+Challenge%3A+Automated+Segmentation+of+Prostate+Structures	No	Unknown
Wang et al. (2021) [102]	10.1016/j. clinimag.2020.10.014	Adam	Learning rate = 0.003 Decay rate = 0.5 Batch size = 8	GTX 1080TI GPU with 64 GB RAM and CUDA edition 9.0 software	http://medicaldecathlon.com/ https://wiki.cancerimagingarchive.net/display/Public/NCI-ISBI+2013+Challenge++Automated+Segmentation+of+Prostate+Structures https://wiki.cancerimagingarchive.net/display/Public/QIN-PROSTATE-Repeatability https://promise12.grand-challenge.org/	Yes	https://github.com/w3user/SegGAN
Kan et al. (2021) [103]	10.1117/12.2582127	Unknown	Unknown	Unknown	Unknown	No	Unknown
Sultana et al. (2020) [104]	10.1117/12.2549979	Unknown	Unknown	Titan Xp GPU	Unknown	No	Unknown
Brion et al. (2021) [105]	10.1016/j. combiomed.2021.104269	Adam	Batch size = 2 Learning rate = 10^{-4} Epoch = 150	Unknown	Unknown	Yes	https://github.com/elliottbrion/unsupervised-domain-adaptation-unet-keras

(continued on next page)

Table A.6 (continued)

Paper	DOI	Optimizer	Hyper-parameter	Training configuration	Data url	Code	Algorithm url
Zhang et al. (2021) [106]	10.1002/mp.14580	Adam	Learning rate = $10^{-2}, 10^{-4}$	Two RTX 2080 Ti GPUs, 8h	Unknown	No	Unknown
Lei et al. (2021) [107]	10.1088/1361-6560/abf2f9	Adam	Learning rate = $2e^{-4}$ Epoch = 400 Batch size = 20	NVIDIA Tesla V100 GPU with 32 GB of memory under the environment of Ubuntu 18.04 LTS	Unknown	No	Unknown

Table A.7

Segmentation GAN-based methods – Spine.

Paper	DOI	Optimizer	Hyper-parameter	Training configuration	Data url	Code	Algorithm url
Han et al. (2018) [108]	10.1016/j.media.2018.08.005	RMSProp Adam	RMSProp Learning rate = 0.01 Decay = 0.9 Momentum = 0.9 $E = 1e^{-10}$ Adam Learning rate = 0.001 $\beta_1 = 0.9 \beta_2 = 0.999$ $E = 1e^{-8}$ Batch size = 4 Epochs = 300	One Nvidia GPU Titan X with cuDNN v5.1 and Intel CPU Xeon(R) @2.5 GHz" title = "mailto:E5-2620@2.5 GHz>E5-2620@2.5 GHz	Unknown	No	Unknown
Sekuboyina et al. (2018) [109]	10.1007/978-3-030-00937-3_74	Adam	Learning rate = 1×10^{-3}	Quadro P5000	Unknown	No	Unknown
Liu. (2019) [110]	10.1002/mrm.27627	Adam	Learning rate = 0.0002	A 64 - bit Ubuntu Linux system, A computer server with an Intel Xeon W3520 quad - core CPU, 32 GB DDR3 RAM, and 1 Nvidia GeForce GTX 1080Ti graphic card with total 3584 CUDA cores, and 11 GB GDDR5 RAM, Time = 6.7 h	http://www.ski10.org/	No	Unknown
Gaj et al. (2020) [111]	10.1002/mrm.28111	Adam	Momentum = 0.5 Learning rate = $1e^{-4}$ Batch size = 10	Owens Cluster with NVIDIA Tesla P100 GPU of Ohio Supercomputer Center	https://nda.nih.gov/oai/	No	Unknown
Kessler et al. (2020) [112]	10.1016/j.compmedimag.2020.101793	Adam	Learning rate = 0.0002 $\beta_1 = 0.5 \beta_2 = 0.999$	Nvidia P6000 GPU card (3840 CUDA cores, 24 GB GDDR5X)	https://ski10.grand-challenge.org/ https://pubdata.zib.de/	No	Unknown
Wei et al. (2020) [113]	10.1063/1.5089738	Adam	$\beta_1 = 0.5 \beta_2 = 0.999$ Learning rate = 0.0002 Batch size = 1 Epochs = 300 Rate in leaky-ReLU = 0.2	NVIDIA DGX-1, equipped with 8 T V100 GPUs, 2 Intel Xeon processors, and 512 GB memory. Time = 5 h 23 min	Unknown	No	Unknown
Alsinan et al. (2020) [114]	10.1007/s11548-020-02221-z	Adam	Learning rate = 0.0002	An Intel Xeon CPU at 3.00 GHz and a Nvidia Titan-X GPU with 8 GB of memory. Train = 8 h Test = 54 ms	Unknown	No	Unknown
Gong et al. (2021) [115]	10.1088/1361-6560/abfad9	Adam	Learning rate = $1e^{-6}$ Batch size = 10	Tesla P100-PCIE GPU with cuDNN v7.1 and Intel CPU Xeon(R) E5 - @2.2" title = "mailto:2650@2.2">2650@2.2 GHz	Unknown	No	Unknown

Table A.8

Segmentation GAN-based methods - Multiple organ.

Paper	DOI	Optimizer	Hyper-parameter	Training configuration	Data url	Code	Algorithm url
Zhang et al. (2018) [116]	10.1007/978-3-030-00934-2_67	Unknown	Unknown	12 GB NVIDIA TITAN X GPU	Unknown	No	Unknown
Tong et al. (2019) [117]	10.1002/mp.13553	Adam	SC-GAN, SRM Batch size = 1, 4 $l_{rs} = 1e^{-3}$ $l_{rd} = 1e^{-4}$ Learning rate = $5e^{-4}$	An NVIDIA GeForce GTX 1080 GPU with 8 GB memory SRM, SC-GAN Time = 2h, 20 h	http://www.imagenglab.com/newsite/pddca/	No	Unknown
Cai et al. (2019) [118]	10.1016/j.media.2018.12.002	Adam	Learning rate = $2e^{-4}$	Unknown	http://medicalresearch.inescporto.pt/breastresearch/index.php/Get_INbreast_Database https://www.bcdr.eu/information/about	No	Unknown
Pang et al. (2020) [119]	10.1007/s00259-020-04781-3	Adam	First 200 epochs Learning rate = $2e^{-4}$ $\alpha = 0 \beta = 1 \gamma = 0$ Next 100 epochs Learning rate = $5e^{-5}$ $\alpha = 1 \beta = 0 \gamma = 100$ Batch size = 1 Momentum = 0.5	A GeForce GTX 1080 graphics card	https://wiki.cancerimagingarchive.net/display/Public/NSCLC-Radiomics . https://github.com/neheller/kits19 .	No	Unknown
Yuan et al. (2020) [120]	10.1016/j.media.2020.101731	Adam	Learning rate = 0.0003 Decays = 3×10^{-7}	Intel i7-8700K CPU and an NVIDIA GTX 1080Ti GPU with 11G memory	https://chaos.grand-challenge.org/Download/ http://medicaldecathlon.com/	No	Unknown
Wang et al. (2020) [121]	10.1109/TMI.2020.3047807	Adam	Learning rate = $5e^{-6}$	Two NVIDIA GTX1080 Ti GPUs	https://www.idiap.ch/software/bob/docs/bob/bob.db.drionsdb/master/index.html https://ieeexplore.ieee.org/document/6867807 https://hc18.grand-challenge.org/ http://db.jsrt.or.jp/eng.php https://www.chaosgroup.com/ https://refuge.grand-challenge.org/ https://ieeexplore.ieee.org/document/6867807 http://cmictig.cs.ucl.ac.uk/niftyweb	No	Unknown
Liu et al. (2021) [122]	10.1016/j.media.2021.102214	Adam SGD	Momentum = 0.9 Learning rate = $2.5 \times 10^{-4}, 1 \times 10^{-4}$	Two Tesla P40 GPUs with 48 GB memory	https://refuge.grand-challenge.org/ https://ieeexplore.ieee.org/document/6867807 http://cmictig.cs.ucl.ac.uk/niftyweb	Yes	https://github.com/zzdxjtu/S-cuda
Dai et al. (2021) [123]	10.1088/1361-6560/abd953	Adam	Epoch = 400 Learning rate = $2e^{-4}$ Batch size = 20	NVIDIA Tesla V100 GPU with 32 GB of memory,6h	Unknown	No	Unknown
Chen et al. (2021) [124]	10.1016/j.media.2021.102060	Adam	Learning rate = 10^{-4} $\lambda 1 = 0.5, \lambda 2 = 0.1, \lambda 3 = 0.1, \lambda 4 = 0.001, \lambda 5 = 0.01, \lambda 6 = 0.01$	Unknown	http://headctstudy.qure.ai/dataset http://adni.loni.usc.edu/ https://zmiclab.github.io/project/smmwhs/	No	Unknown

Table A.9

Segmentation GAN-based methods - Microscopic image.

Paper	DOI	Optimizer	Hyper-parameter	Training configuration	Data url	Code	Algorithm url
Sadanandan et al. (2017) [125]	10.1109/ICCVW.2017.11	Adam	Segmentation net, Adversarial net Learning rate = $10^{-4}, 10^{-3}$ $\text{beta}_1 = 0.5, 0.5$ $\text{beta}_2 = 0.99, 0.99$ Batch size = 1	Workstation with six core Intel(R) Core (TM) i7-5930K CPU running at 3.50 GHz and 32 Gb RAM and a Nvidia Titan X Pascal GPU with 12 Gb GPU memory on Ubuntu 14.04 operating system, Each network took nearly 1 h	Unknown	No	Unknown
Zhang et al. (2017) [126]	10.1007/978-3-319-66179-7_47	Unknown	$\lambda = 0.1$	Unknown	https://warwick.ac.uk/fac/sci/dcs/research/tia/glascontest/	No	Unknown
Arbelle and Raviv (2018) [127]	10.1109/isbi.2018.8363657	Unknown	Unknown	Unknown	http://amp.pharm.mssm.edu/Harmonizome/genome_set/NCI-H1299/COSMIC+Cell+Line+Gene+CNV+Profiles	Yes	https://github.com/arbellea/DeepCellSeg.git
Majurski et al. (2019) [128]	10.1109/CVPRW.2019.00145	Adam	Learning rate = 3×10^{-4}	A single IBM Witherspoon node containing two 20-core IBM Power9 CPUs and four Nvidia V100 GPUs with	https://isg.nist.gov/deepzoomweb/data/RP_Eimplants	No	Unknown

(continued on next page)

Table A.9 (continued)

Paper	DOI	Optimizer	Hyper-parameter	Training configuration	Data url	Code	Algorithm url
Mahmood et al. (2019) [129]	10.1109/TMI.2019.2927182	Adam	$\lambda_n = 70$ $\lambda_m = 10$ Learning rate = 0.0002	NVLink2 interconnection fabric, 3198 min Unknown	https://www.cancer.gov/about-nci/organization/ccg/research/structural-genomics/tcga	Yes	https://github.com/faisalm/NucleiSegmentation
Gadermayr et al. (2019) [130]	10.1109/TMI.2019.2899364	Unknown	Learning rate = 10^{-5} Batch size = 1 Epochs = 15	NVIDIA GeForce GTX 1080 Ti GPU	Unknown	No	Unknown
Guo et al. (2019) [131]	10.1007/978-3-030-17935-9_42	Unknown	Batch size = 128	Unknown	Unknown	No	Unknown
de Bel et al. (2021) [132]	10.1016/j.media.2021.102004	Adam	(colon, kidney) Batch size = 5, 6 Learning rate = 0.0001, 0.0005	Unknown	Unknown	No	Unknown
Liu et al. (2021) [133]	10.1109/TMI.2021.3055483	Adam	Batch size = 32 Learning rate = 0.001	A desktop computer with Microsoft Windows 7, Intel(R) Core (TM) i7-6850K CPU, and dual NVIDIA GeForce GTX 1080 Ti GPUs.	Unknown	No	Unknown
Yang et al. (2021) [134]	10.1109/JBHI.2021.3094520	SGD	Learning rate = 0.01 Momentum = 0.9 Batch size = 2 Epoch = 80 $\beta = 6$	NVIDIA 1660TI GPU with 6 GB memory	Unknown	No	Unknown

Table A.10

Segmentation GAN-based methods – Others.

Paper	DOI	Optimizer	Hyper-parameter	Training configuration	Data url	Code	Algorithm url
Izadi et al. (2018) [135]	10.1109/isbi.2018.8363712	SGD	Unknown	One Titan X (Pascal) GPU using Lasagne, 35 h	https://licensing.edinburgh-innovations.ed.ac.uk/i/software/dermofit-image-library.html	No	Unknown
Xue et al. (2018) [136]	10.1109/isbi.2018.8363707	Adam	Batch size = 25 Learning rate = 0.003	Unknown	https://www.isic-archive.com/#!/topWithHeader/wideContentTop/main	No	Unknown
Lei et al. (2020) [137]	10.1016/j.media.2020.101716	Adam	Batch size = 6 Iterations = 50 Decay = 0.997 Momentum = 0.9 Initial learning rate = 0.007 Final learning rate = 0.000001	On two TITAN XP GPUs	https://www.isic-archive.com/#!/topWithHeader/wideContentTop/main	No	Unknown
Hu et al. (2020) [138]	10.1109/JBHI.2020.2972694	Unknown	Unknown	A GNU/Linux server running Ubuntu 16.04, with Intel Core i7-6700 CPU and 64 GB RAM, A single NVIDIA Titan-Xp GPU with 12 GB RAM	Unknown	No	Unknown
Wang et al. (2020) [139]	10.1364/BOE.394715	Adam	Learning rate = 2×10^{-3}	A 12 GB T K80 GPU using CUDA 9.2 with cuDNN v7	Unknown	No	Unknown
Gadermayr et al. (2019) [140]	10.1002/jmri.26544	Adam	Learning rate = $8e^{-4}$ Batch size = 1 Epochs = 250	Unknown	Unknown	No	Unknown
Nishiyama et al. (2021) [141]	10.1371/journal.pone.0257371	Adam	beta1 = 0.9 L1_weight = 1000	Unknown	Unknown	Yes	https://github.com/affinelayer/pix2pix-tensorflow

References

- [1] G. Litjens, T. Kooi, B.E. Bejnordi, A.A.A. Setio, F. Ciompi, M. Ghafoorian, J.A. Van Der Laak, B. Van Ginneken, C.I. Sánchez, A survey on deep learning in medical image analysis, *Med. Image Anal.* 42 (2017) 60–88.
- [2] I. Goodfellow, J. Pouget-Abadie, M. Mirza, B. Xu, D. Warde-Farley, S. Ozair, A. Courville, Y. Bengio, Generative adversarial nets, in: *Adv. Neural Inf. Process. Syst.*, 2014, pp. 2672–2680.
- [3] S. Kazemnia, C. Baur, A. Kuijper, B. van Ginneken, N. Navab, S. Albarqouni, A. Mukhopadhyay, GANs for medical image analysis, *Artif. Intell. Med.* 109 (2020) 1–40, <https://doi.org/10.1016/j.artmed.2020.101938>.
- [4] X. Yi, E. Walia, P. Babyn, Generative adversarial network in medical imaging: a review, *Med. Image Anal.* 58 (2019), <https://doi.org/10.1016/j.media.2019.101552>.
- [5] A.L. Simpson, M. Antonelli, S. Bakas, M. Bilello, K. Farahani, B. van Ginneken, A. Kopp-Schneider, B.A. Landman, G. Litjens, B. Menze, O. Ronneberger, R. M. Summers, P. Bilic, P.F. Christ, R.K.G. Do, M. Gollub, J. Golia-Pernicka, S. Heckers, W.R. Jarnagin, M.K. McHugo, S. Napel, E. Vorontsov, L. Maier-Hein, M.J. Cardoso, A Large Annotated Medical Image Dataset for the Development and Evaluation of Segmentation Algorithms, 2019, <http://arxiv.org/abs/1902.09063>.
- [6] M. Mirza, S. Osindero, Conditional generative adversarial nets, *ArXiv Prepr. ArXiv1411.1784* (2014).
- [7] A. Radford, L. Metz, S. Chintala, Unsupervised representation learning with deep convolutional generative adversarial networks, *ArXiv Prepr. ArXiv1511.06434* (2015).
- [8] X. Chen, Y. Duan, R. Houthooft, J. Schulman, I. Sutskever, P. Abbeel, Infogan: interpretable representation learning by information maximizing generative adversarial nets, in: *Adv. Neural Inf. Process. Syst.*, 2016, pp. 2172–2180.
- [9] A. Odena, C. Olah, J. Shlens, Conditional image synthesis with auxiliary classifier gans, *Int. Conf. Mach. Learn.* (2017) 2642–2651.
- [10] M. Arjovsky, S. Chintala, L. Bottou, Wasserstein gan, *ArXiv Prepr. ArXiv1701.07875* (2017).
- [11] J.-Y. Zhu, T. Park, P. Isola, A.A. Efros, Unpaired image-to-image translation using cycle-consistent adversarial networks, *Proc. IEEE Int. Conf. Comput. Vis.* (2017) 2223–2232.
- [12] P. Isola, J.-Y. Zhu, T. Zhou, A.A. Efros, Image-to-image translation with conditional adversarial networks, in: *Proc. IEEE Conf. Comput. Vis. Pattern Recognit.*, 2017, pp. 1125–1134.
- [13] O. Ronneberger, P. Fischer, T. Brox, U-net: Convolutional networks for biomedical image segmentation, in: *Int. Conf. Med. Image Comput. Comput. Interv.*, Springer, 2015, pp. 234–241.
- [14] A. Brock, J. Donahue, K. Simonyan, Large scale gan training for high fidelity natural image synthesis, *ArXiv Prepr. ArXiv1809.11096* (2018).
- [15] T. Karras, S. Laine, T. Aila, A style-based generator architecture for generative adversarial networks, in: *Proc. IEEE Conf. Comput. Vis. Pattern Recognit.*, 2019, pp. 4401–4410.
- [16] P. Luc, C. Couprise, S. Chintala, J. Verbeek, Semantic segmentation using adversarial networks, *ArXiv Prepr. ArXiv1611.08408* (2016).
- [17] Z. Li, Y. Wang, J. Yu, Brain tumor segmentation using an adversarial network, *Lect. Notes Comput. Sci. (Including Subser. Lect. Notes Artif. Intell. Lect. Notes Bioinformatics)*. 10670 LNCS (2018) 123–132, https://doi.org/10.1007/978-3-319-75238-9_11.
- [18] M. Rezaei, K. Harmuth, W. Gierke, T. Kellermeier, M. Fischer, H. Yang, C. Meinel, A conditional adversarial network for semantic segmentation of brain tumor, *Lect. Notes Comput. Sci. (Including Subser. Lect. Notes Artif. Intell. Lect. Notes Bioinformatics)*. 10670 LNCS (2018) 241–252, https://doi.org/10.1007/978-3-319-75238-9_21.
- [19] Y. Xue, T. Xu, H. Zhang, L.R. Long, X. Huang, SegAN: adversarial network with multi-scale L 1 loss for medical image segmentation, *Neuroinformatics* 16 (2018) 383–392, <https://doi.org/10.1007/s12021-018-9377-x>.
- [20] W. Yuan, J. Wei, J. Wang, Q. Ma, T. Tasdizen, Unified attentional generative adversarial network for brain tumor segmentation from multimodal unpaired images, *Lect. Notes Comput. Sci. (Including Subser. Lect. Notes Artif. Intell. Lect. Notes Bioinformatics)*. 11766 LNCS (2019) 229–237, https://doi.org/10.1007/978-3-030-32248-9_26.
- [21] S. Nema, A. Dudhane, S. Murala, S. Naidu, RescueNet: an unpaired GAN for brain tumor segmentation, *Biomed. Signal Process Control* 55 (2020) 101641, <https://doi.org/10.1016/j.bspc.2019.101641>.
- [22] Y. Li, Y. Chen, Y. Shi, Brain tumor segmentation using 3D generative adversarial networks, *Int. J. Pattern Recogn. Artif. Intell.* 35 (2021), <https://doi.org/10.1142/S0218001421570020>.
- [23] G.M. Conte, A.D. Weston, D.C. Vogelsang, K.A. Philbrick, J.C. Cai, Erratum: generative adversarial networks to synthesize missing T1 and FLAIR MRI sequences for use in a multisequence brain tumor segmentation model, *Radiology* 300 (2021) E319, <https://doi.org/10.1148/radiol.2021219009>. Radiology (2021) 299:2 (313–323) DOI: 10.1148/radiol.2021203786.
- [24] G. Cheng, H. Ji, L. He, Correcting and reweighting false label masks in brain tumor segmentation, *Med. Phys.* 48 (2021) 169–177, <https://doi.org/10.1002/mp.14480>.
- [25] P. Moeskops, M. Veta, M.W. Lafarge, K.A.J. Eppenhof, J.P.W. Pluim, Adversarial training and dilated convolutions for brain MRI segmentation, in: *Deep Learn. Med. Image Anal. Multimodal Learn. Clin. Decis. Support*, Springer, 2017, pp. 56–64.
- [26] A.K. Mondal, J. Dolz, C. Desrosiers, Few-shot 3d multi-modal medical image segmentation using generative adversarial learning, *ArXiv Prepr. ArXiv1810.12241* (2018).
- [27] K.T. Oh, S. Lee, H. Lee, M. Yun, S.K. Yoo, Semantic segmentation of white matter in FDG-PET using generative adversarial network, *J. Digit. Imag.* (2020) 1–10.
- [28] P.L. Delisle, B. Anctil-Robitaille, C. Desrosiers, H. Lombaert, Realistic image normalization for multi-Domain segmentation, *Med. Image Anal.* 74 (2021) 102191, <https://doi.org/10.1016/j.media.2021.102191>.
- [29] M. Zhao, L. Wang, J. Chen, D. Nie, Y. Cong, S. Ahmad, A. Ho, P. Yuan, S.H. Fung, H.H. Deng, Craniomaxillofacial bony structures segmentation from MRI with deep-supervision adversarial learning, in: *Int. Conf. Med. Image Comput. Comput. Interv.*, Springer, 2018, pp. 720–727.
- [30] X. Chen, C. Lian, L. Wang, H. Deng, S.H. Fung, D. Nie, K.-H. Thung, P.-T. Yap, J. Gateno, J.J. Xia, One-Shot generative adversarial learning for MRI segmentation of craniomaxillofacial bony structures, *IEEE Trans. Med. Imag.* 39 (2019) 787–796.
- [31] Y. Shi, K. Cheng, Z. Liu, Hippocampal subfields segmentation in brain MR images using generative adversarial networks, *Biomed. Eng. Online* 18 (2019) 1–12.
- [32] Q. Delannoy, C.H. Pham, C. Cazorla, C. Tor-Díez, G. Dollé, H. Meunier, N. Bednarek, R. Fablet, N. Passat, SegSRGAN: super-resolution and segmentation using generative adversarial networks — application to neonatal brain MRI, *Comput. Biol. Med.* 120 (2020) 103755, <https://doi.org/10.1016/j.combiomed.2020.103755>.
- [33] B. Li, X. You, J. Wang, Q. Peng, S. Yin, R. Qi, Q. Ren, Z. Hong, IAS-NET: joint Intra-classly Adaptive GAN and Segmentation network for unsupervised cross-domain in Neonatal Brain MRI segmentation, *Med. Phys.* (2021), <https://doi.org/10.1002/mp.15212>.
- [34] V. Alex, M.S. Kp, S.S. Chennamsetty, G. Krishnamurthy, Generative adversarial networks for brain lesion detection, in: *Med. Imaging 2017 Image Process*, International Society for Optics and Photonics, 2017, p. 101330G.
- [35] K. Kamnitsas, C. Baumgartner, C. Ledig, V. Newcombe, J. Simpson, A. Kane, D. Menon, A. Nori, A. Criminisi, D. Rueckert, B. Glocker, Unsupervised domain adaptation in brain lesion segmentation with adversarial networks, in: *Lect. Notes Comput. Sci. (Including Subser. Lect. Notes Artif. Intell. Lect. Notes Bioinformatics)*, 10265, LNCS, 2017, pp. 597–609, https://doi.org/10.1007/978-3-319-59050-9_47.
- [36] H. Kuang, B.K. Menon, W. Qiu, Automated stroke lesion segmentation in non-contrast CT scans using dense multi-path contextual generative adversarial network, *Phys. Med. Biol.* 65 (2020), <https://doi.org/10.1088/1361-6560/aba166>.
- [37] T. Finck, H. Li, L. Grundl, P. Eichinger, M. Bussas, M. Mühlau, B. Menze, B. Wiestler, Deep-learning generated synthetic double inversion recovery images improve multiple sclerosis lesion detection, *Invest. Radiol.* 55 (2020) 318–323, <https://doi.org/10.1097/RLI.0000000000000640>.
- [38] F. La Rosa, T. Yu, G. Barqueró, J.P. Thiran, C. Granziera, M. Bach Cuadra, MPRAGE to MP2RAGE UNI translation via generative adversarial network improves the automatic tissue and lesion segmentation in multiple sclerosis patients, *Comput. Biol. Med.* 132 (2021), <https://doi.org/10.1016/j.combiomed.2021.104297>.
- [39] A. Lahiri, K. Ayush, P. Kumar Biswas, P. Mitra, Generative adversarial learning for reducing manual annotation in semantic segmentation on large scale microscopy images: automated vessel segmentation in retinal fundus image as test case, in: *Proc. IEEE Conf. Comput. Vis. Pattern Recognit. Work.*, 2017, pp. 42–48.
- [40] D. Mahapatra, B. Bozorgtabar, S. Hewavitharanage, R. Garnavi, Image super resolution using generative adversarial networks and local saliency maps for retinal image analysis, in: *Int. Conf. Med. Image Comput. Comput. Interv.*, Springer, 2017, pp. 382–390.
- [41] M. Javanmardi, T. Tasdizen, Domain adaptation for biomedical image segmentation using adversarial training, *Proc. Int. Symp. Biomed. Imaging.* (2018) 554–558, <https://doi.org/10.1109/ISBI.2018.8363637>, 2018-April.
- [42] T. Iqbal, H. Ali, Generative adversarial network for medical images (MI-GAN), *J. Med. Syst.* 42 (2018) 231.
- [43] J. Son, S.J. Park, K.H. Jung, Towards accurate segmentation of retinal vessels and the optic disc in fundoscopic images with generative adversarial networks, *J. Digit. Imag.* 32 (2019) 499–512, <https://doi.org/10.1007/s10278-018-0126-3>.
- [44] T. Yang, T. Wu, L. Li, C. Zhu, SUD-GAN: Deep convolution generative adversarial network combined with short connection and dense block for retinal vessel segmentation, *J. Digit. Imag.* (2020) 1–12.
- [45] T. Schlegl, P. Seeböck, S.M. Waldstein, U. Schmidt-Erfurth, G. Langs, Unsupervised anomaly detection with generative adversarial networks to guide marker discovery, in: *Int. Conf. Inf. Process. Med. Imaging*, Springer, 2017, pp. 146–157.
- [46] H. Jiang, X. Chen, F. Shi, Y. Ma, D. Xiang, L. Ye, J. Su, Z. Li, Q. Chen, Y. Hua, X. Xu, W. Zhu, Y. Fan, Improved cGAN based linear lesion segmentation in high myopia ICGA images, *Biomed. Opt Express* 10 (2019) 2355, <https://doi.org/10.1364/boe.10.002355>.
- [47] T. Schlegl, P. Seeböck, S.M. Waldstein, G. Langs, U. Schmidt-Erfurth, f-AnoGAN, Fast unsupervised anomaly detection with generative adversarial networks, *Med. Image Anal.* 54 (2019) 30–44, <https://doi.org/10.1016/j.media.2019.01.010>.
- [48] J. Wang, W. Li, Y. Chen, W. Fang, W. Kong, Y. He, G. Shi, Weakly supervised anomaly segmentation in retinal OCT images using an adversarial learning approach, *Biomed. Opt Express* 12 (2021) 4713, <https://doi.org/10.1364/boe.426803>.
- [49] S.M. Shankaranarayana, K. Ram, K. Mitra, M. Sivaprakasam, Joint optic disc and cup segmentation using fully convolutional and adversarial networks, *Lect. Notes Comput. Sci. (Including Subser. Lect. Notes Artif. Intell. Lect. Notes Bioinformatics)*. 10554 LNCS (2017) 168–176, https://doi.org/10.1007/978-3-319-67561-9_19.

- [50] S. Wang, L. Yu, X. Yang, C.-W. Fu, P.-A. Heng, Patch-based output space adversarial learning for joint optic disc and cup segmentation, *IEEE Trans. Med. Imag.* 38 (2019) 2485–2495.
- [51] S. Kadambi, Z. Wang, E. Xing, WGAN domain adaptation for the joint optic disc-and-cup segmentation in fundus images, *Int. J. Comput. Assist. Radiol. Surg.* (2020).
- [52] L. Luo, D. Xue, F. Pan, X. Feng, Joint optic disc and optic cup segmentation based on boundary prior and adversarial learning, *Int. J. Comput. Assist. Radiol. Surg.* 16 (2021) 905–914, <https://doi.org/10.1007/s11548-021-02373-6>.
- [53] X. Liu, J. Cao, T. Fu, Z. Pan, W. Hu, K. Zhang, J. Liu, Semi-supervised automatic segmentation of layer and fluid region in retinal optical coherence tomography images using adversarial learning, *IEEE Access* 7 (2019) 3046–3061, <https://doi.org/10.1109/ACCESS.2018.2889321>.
- [54] R. Tennakoon, A.K. Gostar, R. Hoseinnezhad, A. Bab-Hadiashar, Retinal fluid segmentation in OCT images using adversarial loss based convolutional neural networks, *Proc. Int. Symp. Biomed. Imaging.* (2018) 1436–1440, <https://doi.org/10.1109/ISBI.2018.8363842>, 2018-April.
- [55] H. Jiang, Y. Ma, W. Zhu, Y. Fan, Y. Hua, Q. Chen, X. Chen, cGAN-based lacquer cracks segmentation in ICGA image, in: *Comput. Pathol. Ophthalmic Med. Image Anal.*, Springer, 2018, pp. 228–235.
- [56] J. Ouyang, T.S. Mathai, K. Lathrop, J. Galeotti, Accurate tissue interface segmentation via adversarial pre-segmentation of anterior segment OCT images, *Biomed. Opt Express* 10 (2019) 5291, <https://doi.org/10.1364/boe.10.005291>.
- [57] E. Yıldız, A.T. Arslan, A.Y. Taş, A.F. Acer, S. Demir, A. Şahin, D.E. Barkana, Generative adversarial network based automatic segmentation of corneal subbasal nerves on *in vivo* confocal microscopy images, *Transl. Vis. Sci. Technol.* 10 (2021) 1–13, <https://doi.org/10.1167/tvst.10.6.33>.
- [58] W. Zhu, X. Xiang, T.D. Tran, X. Xie, Adversarial Deep Structural Networks for Mammographic Mass Segmentation, 2016, pp. 1–8, <https://doi.org/10.1101/095786>.
- [59] T. Shen, C. Gou, F.Y. Wang, Z. He, W. Chen, Learning from adversarial medical images for X-ray breast mass segmentation, *Comput. Methods Progr. Biomed.* 180 (2019) 1–13, <https://doi.org/10.1016/j.cmpb.2019.105012>.
- [60] L. Han, Y. Huang, H. Dou, S. Wang, S. Ahamed, H. Luo, Q. Liu, J. Fan, J. Zhang, Semi-supervised segmentation of lesion from breast ultrasound images with attentional generative adversarial network, *Comput. Methods Progr. Biomed.* 189 (2020) 105275, <https://doi.org/10.1016/j.cmpb.2019.105275>.
- [61] J. Xing, Z. Li, B. Wang, Y. Qi, B. Yu, F.G. Zanjani, A. Zheng, R. Duits, T. Tan, Lesion segmentation in ultrasound using semi-pixel-wise cycle generative adversarial nets, *IEEE ACM Trans. Comput. Biol. Bioinf.* (2020).
- [62] X. Ma, J. Wang, X. Zheng, Z. Liu, W. Long, Y. Zhang, et al., Automated fibroglandular tissue segmentation in breast MRI using generative adversarial networks, *Phys. Med. Biol.* 65 (2020) 105006.
- [63] Y. Li, G. Zhao, Q. Zhang, Y. Lin, M. Wang, SAP-cGAN: adversarial learning for breast mass segmentation in digital mammogram based on superpixel average pooling, *Med. Phys.* 48 (2021) 1157–1167, <https://doi.org/10.1002/mp.14671>.
- [64] C. Chen, Q. Dou, H. Chen, P.-A. Heng, Semantic-aware generative adversarial nets for unsupervised domain adaptation in chest x-ray segmentation, in: *Int. Work. Mach. Learn. Med. Imaging*, Springer, 2018, pp. 143–151.
- [65] J. Tan, L. Jing, Y. Huo, L. Li, O. Akin, Y. Tian, LGAN: lung segmentation in CT scans using generative adversarial network, *Comput. Med. Imag. Graph.* 87 (2021) 101817, <https://doi.org/10.1016/j.compmedimag.2020.101817>.
- [66] B. Stiehl, M. Lauria, K. Singhrao, J. Goldin, I. Barjaktarevic, D. Low, A. Santhanam, Scalable quorom-based deep neural networks with adversarial learning for automated lung lobe segmentation in fast helical free-breathing CTs, *Int. J. Comput. Assist. Radiol. Surg.* (2021), <https://doi.org/10.1007/s11548-021-02454-6>.
- [67] D. Jin, Z. Xu, Y. Tang, A.P. Harrison, D.J. Mollura, CT-realistic lung nodule simulation from 3D conditional generative adversarial networks for robust lung segmentation, in: *Int. Conf. Med. Image Comput. Comput. Interv.*, Springer, 2018, pp. 732–740.
- [68] S. Jain, S. Indora, D.K. Atal, Lung nodule segmentation using salp shuffled shepherd optimization algorithm-based generative adversarial network, *Comput. Biol. Med.* 137 (2021) 104811, <https://doi.org/10.1016/j.combiomed.2021.104811>.
- [69] W. Dai, N. Dong, Z. Wang, X. Liang, H. Zhang, E.P. Xing, Scan: Structure Correcting Adversarial Network for Organ Segmentation in Chest X-Rays, Springer International Publishing, 2018, https://doi.org/10.1007/978-3-030-00889-5_30.
- [70] R. Trullo, C. Petitjean, B. Dubray, S. Ruan, Multiorgan segmentation using distance-aware adversarial networks, *J. Med. Imaging* 6 (2019) 14001.
- [71] X. Dong, Y. Lei, T. Wang, M. Thomas, L. Tang, W.J. Curran, T. Liu, X. Yang, Automatic multiorgan segmentation in thorax CT images using U-net-GAN, *Med. Phys.* 46 (2019) 2157–2168.
- [72] Y. Guo, W. Zhao, S. Li, Y. Zhang, Y. Lu, Automatic segmentation of the pectoral muscle based on boundary identification and shape prediction, *Phys. Med. Biol.* 65 (2020), <https://doi.org/10.1088/1361-6560/ab652b>.
- [73] Q. Dou, C. Ouyang, C. Chen, H. Chen, P.A. Heng, Unsupervised cross-modality domain adaptation of convnets for biomedical image segmentations with adversarial loss, *IJCAI Int. Jt. Conf. Artif. Intell.* (2018) 691–697, <https://doi.org/10.24963/ijcai.2018/96>, 2018-July.
- [74] M. Rezaei, H. Yang, C. Meinel, Whole heart and great vessel segmentation with context-aware of generative adversarial networks, in: *Bild. Für Die Medizin* 2018, Springer, 2018, pp. 353–358.
- [75] Z. Zhang, L. Yang, Y. Zheng, Translating and segmenting multimodal medical volumes with cycle-and shape-consistency generative adversarial network, in: *Proc. IEEE Conf. Comput. Vis. Pattern Recognit.*, 2018, pp. 9242–9251.
- [76] T. Joyce, A. Chartsias, S.A. Tsafaris, Deep Multi-Class Segmentation without Ground-Truth Labels, 2018.
- [77] S. Dong, G. Luo, K. Wang, S. Cao, A. Mercado, O. Shmuelovich, H. Zhang, S. Li, VoxelAtlasGAN: 3D left ventricle segmentation on echocardiography with atlas guided generation and voxel-to-voxel discrimination, in: *Int. Conf. Med. Image Comput. Comput. Interv.*, Springer, 2018, pp. 622–629.
- [78] A. Chartsias, T. Joyce, G. Papanastasiou, S. Semple, M. Williams, D. Newby, R. Dharmakumar, S.A. Tsafaris, Factorised Spatial Representation Learning: Application in Semi-supervised Myocardial Segmentation, Springer International Publishing, 2018, https://doi.org/10.1007/978-3-030-00934-2_55.
- [79] J. Liu, H. Xie, S. Zhang, L. Gu, Multi-sequence myocardium segmentation with cross-constrained shape and neural network-based initialization, *Comput. Med. Imag. Graph.* 71 (2019) 49–57, <https://doi.org/10.1016/j.compmedimag.2018.11.001>.
- [80] R.R. Upendra, S. Dangi, C.A. Linte, An adversarial network architecture using 2D U-net models for segmentation of left ventricle from cine cardiac MRI, *Funct. Imag. Model Heart* 11504 (2019 Jun) 415–424, https://doi.org/10.1007/978-3-030-21949-9_45.
- [81] C. Xu, J. Howey, P. Ohorodnyk, M. Roth, H. Zhang, S. Li, Segmentation and quantification of infarction without contrast agents via spatiotemporal generative adversarial learning, *Med. Image Anal.* 59 (2020) 101568, <https://doi.org/10.1016/j.media.2019.101568>.
- [82] C. Decourt, L. Duong, Semi-supervised generative adversarial networks for the segmentation of the left ventricle in pediatric MRI, *Comput. Biol. Med.* 123 (2020) 103884.
- [83] X. Shi, T. Du, S. Chen, H. Zhang, C. Guan, B. Xu, UENet: a novel generative adversarial network for angiography image segmentation, in: *2020 42nd Annu. Int. Conf. IEEE Eng. Med. Biol. Soc.*, IEEE, 2020, pp. 1612–1615.
- [84] H. Cui, C. Yuwen, L. Jiang, Y. Xia, Y. Zhang, Bidirectional cross-modality unsupervised domain adaptation using generative adversarial networks for cardiac image segmentation, *Comput. Biol. Med.* 136 (2021) 104726, <https://doi.org/10.1016/j.combiomed.2021.104726>.
- [85] H. Wu, X. Lu, B. Lei, Z. Wen, Automated left ventricular segmentation from cardiac magnetic resonance images via adversarial learning with multi-stage pose estimation network and co-discriminator, *Med. Image Anal.* 68 (2021) 101891, <https://doi.org/10.1016/j.media.2020.101891>.
- [86] X. Yang, Y. Zhang, B. Lo, D. Wu, H. Liao, Y.T. Zhang, DBAN: adversarial network with multi-scale features for cardiac MRI segmentation, *IEEE J. Biomed. Heal. Inf.* 25 (2021), <https://doi.org/10.1109/JBHI.2020.3028463>, 2018–2028.
- [87] J. Chen, G. Yang, H. Khan, H. Zhang, Y. Zhang, S. Zhao, R. Mohiaddin, T. Wong, D. Firmin, J. Keegan, JAS-GAN: Generative adversarial network based joint atrium and scar segmentation on unbalanced atrial targets, *IEEE J. Biomed. Heal. Informatics.* 2194 (2021) 1–13, <https://doi.org/10.1109/JBHI.2021.3077469>.
- [88] A. Gilbert, M. Marciniak, C. Rodero, P. Lamata, E. Samset, K. McLeod, Generating synthetic labeled data from existing anatomical models: an example with echocardiography segmentation, *IEEE Trans. Med. Imag.* 40 (2021) 2783–2794, <https://doi.org/10.1109/TMI.2021.3051806>.
- [89] D. Yang, D. Xu, S.K. Zhou, B. Georgescu, M. Chen, S. Grbic, D. Metaxas, D. Comaniciu, Automatic liver segmentation using an adversarial image-to-image network, *Int. Conf. Med. Image Comput. Comput. Interv.* (2017) 507–515, <https://doi.org/10.1007/978-3-319-66179-7>.
- [90] B. Kim, J.C. Ye, Cycle-consistent Adversarial Network with Polyphase U-Nets for Liver Lesion Segmentation, 2018.
- [91] Y. Huo, Z. Xu, S. Bao, C. Bermudez, A.J. Plassard, Y. Yao, J. Liu, A. Assad, R. G. Abramson, B.A. Landman, Splenomegaly Segmentation Using Global Convolutional Kernels and Conditional Generative Adversarial Networks, vol. 8, 2018, <https://doi.org/10.1117/12.2293406>.
- [92] Y. Huo, Z. Xu, S. Bao, A. Assad, R.G. Abramson, B.A. Landman, Adversarial synthesis learning enables segmentation without target modality ground truth, *Proc. - Int. Symp. Biomed. Imaging.* (2018) 1217–1220, <https://doi.org/10.1109/ISBI.2018.8363790>, 2018-April.
- [93] X. Liu, S. Guo, H. Zhang, K. He, S. Mu, Y. Guo, X. Li, Accurate colorectal tumor segmentation for CT scans based on the label assignment generative adversarial network, *Med. Phys.* 46 (2019) 3532–3542.
- [94] J.M. Poomeshwaran, K.S. Santhosh, K. Ram, J. Joseph, M. Sivaprakasam, Polyp segmentation using generative adversarial network, *Proc. Annu. Int. Conf. IEEE Eng. Med. Biol. Soc. EMBS.* (2019) 7201–7204, <https://doi.org/10.1109/EMBC.2019.8857958>.
- [95] Y. Ruan, D. Li, H. Marshall, T. Miao, T. Cossetto, I. Chan, O. Daher, F. Accorsi, A. Goela, S. Li, MB-FSGAN: Joint segmentation and quantification of kidney tumor on CT by the multi-branch feature sharing generative adversarial network, *Med. Image Anal.* (2020) 101721.
- [96] L. Huang, M. Li, S. Gou, X. Zhang, K. Jiang, Automated segmentation method for low field 3D stomach MRI using transferred learning image enhancement network, *BioMed Res. Int.* 2021 (2021).
- [97] M. Li, F. Lian, C. Wang, S. Guo, Dual adversarial convolutional networks with multilevel cues for pancreatic segmentation, *Phys. Med. Biol.* 66 (2021) 175025, <https://doi.org/10.1088/1361-6560/ac155f>.
- [98] V. Sandfort, K. Yan, P.J. Pickhardt, R.M. Summers, Data augmentation using generative adversarial networks (CycleGAN) to improve generalizability in CT segmentation tasks, *Sci. Rep.* 9 (2019) 1–9, <https://doi.org/10.1038/s41598-019-52737-x>.

- [99] P.H. Conze, A.E. Kavur, E. Corne Le Gall, N.S. Gezer, Y. Le Meur, M.A. Selver, F. Rousseau, Abdominal multi-organ segmentation with cascaded convolutional and adversarial deep networks, *Artif. Intell. Med.* 117 (2021) 102109, <https://doi.org/10.1016/j.artmed.2021.102109>.
- [100] S. Kohl, D. Bonekamp, H.-P. Schlemmer, K. Yaqubi, M. Hohenfellner, B. Hadischik, J.-P. Radtke, K. Maier-Hein, Adversarial Networks for the Detection of Aggressive Prostate Cancer, 2017, 08014. ArXiv Prepr. ArXiv1702.
- [101] H. Jia, Y. Xia, Y. Song, D. Zhang, H. Huang, Y. Zhang, W. Cai, 3D APA-Net: 3D adversarial pyramid anisotropic convolutional network for prostate segmentation in MR images, *IEEE Trans. Med. Imag.* 39 (2019) 447–457.
- [102] W. Wang, G. Wang, X. Wu, X. Ding, X. Cao, L. Wang, J. Zhang, P. Wang, Automatic segmentation of prostate magnetic resonance imaging using generative adversarial networks, *Clin. Imag.* 70 (2021) 1–9, <https://doi.org/10.1016/j.clinimag.2020.10.014>.
- [103] C.N.E. Kan, T. Gilat-Schmidt, D.H. Ye, Enhancing reproductive organ segmentation in pediatric CT via adversarial learning, 1, 2021, p. 31, <https://doi.org/10.1111/12.2582127>.
- [104] S. Sultana, A. Robinson, D.Y. Song, J. Lee, CNN-based Hierarchical Coarse-To-Fine Segmentation of Pelvic CT Images for Prostate Cancer Radiotherapy, 2020, p. 53, <https://doi.org/10.1117/12.2549979>.
- [105] E. Brion, J. Léger, A.M. Barragán-Montero, N. Meert, J.A. Lee, B. Macq, Domain adversarial networks and intensity-based data augmentation for male pelvic organ segmentation in cone beam CT, *Comput. Biol. Med.* 131 (2021), <https://doi.org/10.1016/j.combiomed.2021.104269>.
- [106] Z. Zhang, T. Zhao, H. Gay, W. Zhang, B. Sun, ARPM-net: a novel CNN-based adversarial method with Markov random field enhancement for prostate and organs at risk segmentation in pelvic CT images, *Med. Phys.* 48 (2021) 227–237, <https://doi.org/10.1002/mp.14580>.
- [107] Y. Lei, T. Wang, S. Tian, Y. Fu, P. Patel, A.B. Jani, W.J. Curran, T. Liu, X. Yang, Male pelvic CT multi-organ segmentation using synthetic MRI-aided dual pyramid networks, *Phys. Med. Biol.* 66 (2021), <https://doi.org/10.1088/1361-6560/abf2f9>.
- [108] Z. Han, B. Wei, A. Mercado, S. Leung, S. Li, Spine-GAN: semantic segmentation of multiple spinal structures, *Med. Image Anal.* 50 (2018) 23–35, <https://doi.org/10.1016/j.media.2018.08.005>.
- [109] A. Sekuboina, M. Rempfler, J. Kukacka, G. Tetteh, A. Valentinitisch, J. S. Kirschke, B.H. Menze, Btrfly net: vertebrae labelling with energy-based adversarial learning of local spine prior, in: *Int. Conf. Med. Image Comput. Comput. Interv.*, Springer, 2018, pp. 649–657.
- [110] F. Liu, SUSAN: segment unannotated image structure using adversarial network, *Magn. Reson. Med.* 81 (2019) 3330–3345, <https://doi.org/10.1002/mrm.27627>.
- [111] S. Gaj, M. Yang, K. Nakamura, X. Li, Automated cartilage and meniscus segmentation of knee MRI with conditional generative adversarial networks, *Magn. Reson. Med.* 84 (2020) 437–449, <https://doi.org/10.1002/mrm.28111>.
- [112] D.A. Kessler, J.W. MacKay, V.A. Crowe, F.M.D. Henson, M.J. Graves, F.J. Gilbert, J.D. Kaggie, The optimisation of deep neural networks for segmenting multiple knee joint tissues from MRIs, *Comput. Med. Imag. Graph.* 86 (2020) 101793.
- [113] Q. Wei, J. Han, Y. Jia, L. Zhu, S. Zhang, Y. Lu, B. Yang, S. Tang, An approach for fully automatic femoral neck-shaft angle evaluation on radiographs, *Rev. Sci. Instrum.* 91 (2020), <https://doi.org/10.1063/1.5089738>.
- [114] A.Z. Alsinan, V.M. Patel, I. Hacihaliloglu, Bone shadow segmentation from ultrasound data for orthopedic surgery using GAN, *Int. J. Comput. Assist. Radiol. Surg.* 15 (2020) 1477–1485.
- [115] H. Gong, J. Liu, S. Li, B. Chen, Axial-SpineGAN: simultaneous segmentation and diagnosis of multiple spinal structures on axial magnetic resonance imaging images, *Phys. Med. Biol.* 66 (2021), <https://doi.org/10.1088/1361-6560/abfad9>.
- [116] Y. Zhang, S. Miao, T. Mansi, R. Liao, Task driven generative modeling for unsupervised domain adaptation: application to x-ray image segmentation, in: *Int. Conf. Med. Image Comput. Comput. Interv.*, Springer, 2018, pp. 599–607.
- [117] N. Tong, S. Gou, S. Yang, M. Cao, K. Sheng, Shape constrained fully convolutional DenseNet with adversarial training for multiorgan segmentation on head and neck CT and low-field MR images, *Med. Phys.* 46 (2019) 2669–2682.
- [118] J. Cai, Z. Zhang, L. Cui, Y. Zheng, L. Yang, Towards cross-modal organ translation and segmentation: a cycle- and shape-consistent generative adversarial network, *Med. Image Anal.* 52 (2019) 174–184, <https://doi.org/10.1016/j.media.2018.12.002>.
- [119] S. Pang, A. Du, M.A. Orgun, Z. Yu, Y. Wang, Y. Wang, G. Liu, CTumorGAN: a unified framework for automatic computed tomography tumor segmentation, *Eur. J. Nucl. Med. Mol. Imag.* (2020) 1–21.
- [120] W. Yuan, J. Wei, J. Wang, Q. Ma, T. Tasdizen, Unified generative adversarial networks for multimodal segmentation from unpaired 3D medical images, *Med. Image Anal.* 64 (2020) 101731, <https://doi.org/10.1016/j.media.2020.101731>.
- [121] L. Wang, D. Guo, G. Wang, S. Zhang, Annotation-efficient learning for medical image segmentation based on noisy pseudo labels and adversarial learning, *IEEE Trans. Med. Imag.* (2020).
- [122] L. Liu, Z. Zhang, S. Li, K. Ma, Y. Zheng, S-CUDA: Self-cleansing unsupervised domain adaptation for medical image segmentation, *Med. Image Anal.* 74 (2021) 102214, <https://doi.org/10.1016/j.media.2021.102214>.
- [123] X. Dai, Y. Lei, T. Wang, A.H. Dhabaan, M. McDonald, J.J. Beitler, W.J. Curran, J. Zhou, T. Liu, X. Yang, Head-and-neck organs-at-risk auto-delineation using dual pyramid networks for CBCT-guided adaptive radiotherapy, *Phys. Med. Biol.* 66 (2021), <https://doi.org/10.1088/1361-6560/abd953>.
- [124] X. Chen, C. Lian, L. Wang, H. Deng, T. Kuang, S.H. Fung, J. Gateno, D. Shen, J. J. Xia, P.T. Yap, Diverse data augmentation for learning image segmentation with cross-modality annotations, *Med. Image Anal.* 71 (2021) 102060, <https://doi.org/10.1016/j.media.2021.102060>.
- [125] S.K. Sadanandan, J. Karlsson, C. Wählby, Spheroid segmentation using multiscale deep adversarial networks, in: *Proc. 2017 IEEE Int. Conf. Comput. Vis. Work. ICCVW*, 2017, pp. 36–41, <https://doi.org/10.1109/ICCVW.2017.11>, 2017. 2018-January.
- [126] Y. Zhang, L. Yang, J. Chen, M. Fredericksen, D.P. Hughes, D.Z. Chen, Deep adversarial networks for biomedical image segmentation utilizing unannotated images, *Lect. Notes Comput. Sci. (Including Subser. Lect. Notes Artif. Intell. Lect. Notes Bioinformatics)*. 10435 LNCS (2017) 408–416, https://doi.org/10.1007/978-3-319-66179-7_47.
- [127] A. Arbelle, T.R. Raviv, Microscopy cell segmentation via adversarial neural networks, in: *2018 IEEE 15th Int. Symp. Biomed. Imaging (ISBI 2018)*, IEEE, 2018, pp. 645–648.
- [128] M. Majurski, P. Manescu, S. Padi, N. Schaub, N. Hotaling, C. Simon Jr., P. Bajcsy, Cell image segmentation using generative adversarial networks, transfer learning, and augmentations, *Proc. IEEE Conf. Comput. Vis. Pattern Recognit. Work.* (2019), 0.
- [129] F. Mahmood, D. Borders, R. Chen, G.N. McKay, K.J. Salimian, A. Baras, N.J. Durr, Deep adversarial training for multi-organ nuclei segmentation in histopathology images, *IEEE Trans. Med. Imag.* (2019).
- [130] M. Gadermayr, L. Gupta, V. Appel, P. Boor, B.M. Klinkhammer, D. Merhof, Generative adversarial networks for facilitating stain-independent supervised and unsupervised segmentation: a study on kidney histology, *IEEE Trans. Med. Imag.* 38 (2019) 2293–2302, <https://doi.org/10.1109/TMI.2019.2899364>.
- [131] Y. Guo, Q. Wang, O. Krupa, J. Stein, G. Wu, K. Bradford, A. Krishnamurthy, Cross modality microscopy segmentation via adversarial adaptation, *Bioinforma. Biomed. Eng. IWBBIO* 2019. *Lect. Notes Comput. Sci.* (2019) 469–478, https://doi.org/10.1007/978-3-030-17935-9_42.
- [132] T. de Bel, J.M. Bokhorst, J. van der Laak, G. Litjens, Residual cyclegan for robust domain transformation of histopathological tissue slides, *Med. Image Anal.* 70 (2021) 102004, <https://doi.org/10.1016/j.media.2021.102004>.
- [133] J. Liu, C. Shen, N. Aguilera, C. Cukras, R.B. Hufnagel, W.M. Zein, T. Liu, J. Tam, Active cell appearance model induced generative adversarial networks for annotation-efficient cell segmentation and identification on adaptive optics retinal images, *IEEE Trans. Med. Imag.* (2021).
- [134] C. Yang, X. Zhou, W. Zhu, D. Xiang, Z. Chen, J. Yuan, X. Chen, F. Shi, Multi-discriminator adversarial convolutional network for nerve fiber segmentation in confocal corneal microscopy images, *IEEE J. Biomed. Heal. Inf.* 2194 (2021), <https://doi.org/10.1109/jbhi.2021.3094520>, 1–1.
- [135] S. Izadi, Z. Mirikhrajai, J. Kawahara, G. Hamarneh, Generative adversarial networks to segment skin lesions, in: *2018 IEEE 15th Int. Symp. Biomed. Imaging (ISBI 2018)*, IEEE, 2018, pp. 881–884.
- [136] Y. Xue, T. Xu, X. Huang, Adversarial learning with multi-scale loss for skin lesion segmentation, *Proc. Int. Symp. Biomed. Imaging* (2018) 859–863, <https://doi.org/10.1109/ISBI.2018.8363707>, 2018-April.
- [137] B. Lei, Z. Xia, F. Jiang, X. Jiang, Z. Ge, Y. Xu, J. Qin, S. Chen, T. Wang, S. Wang, Skin lesion segmentation via generative adversarial networks with dual discriminators, *Med. Image Anal.* (2020) 101716.
- [138] X. Hu, R. Guo, J. Chen, H. Li, D. Waldmannstetter, Y. Zhao, B. Li, K. Shi, B. Menze, Coarse-to-Fine adversarial networks and zone-based uncertainty analysis for NK/T-cell lymphoma segmentation in CT/PET images, *IEEE J. Biomed. Heal. Inf.* (2020).
- [139] C. Wang, M. Gan, M. Zhang, D. Li, Adversarial convolutional network for esophageal tissue segmentation on OCT images, *Biomed. Opt Express* 11 (2020) 3095, <https://doi.org/10.1364/boe.394715>.
- [140] M. Gadermayr, K. Li, M. Müller, D. Truhn, N. Krämer, D. Merhof, B. Gess, Domain-specific data augmentation for segmenting MR images of fatty infiltrated human thighs with neural networks, *J. Magn. Reson. Imag.* 49 (2019) 1676–1683, <https://doi.org/10.1002/jmri.26544>.
- [141] D. Nishiyama, H. Iwasaki, T. Taniguchi, D. Fukui, M. Yamanaka, T. Harada, H. Yamada, Deep generative models for automated muscle segmentation in computed tomography scanning, *PLoS One* 16 (2021), e0257371, <https://doi.org/10.1371/journal.pone.0257371>.
- [142] Y. Qin, H. Zheng, X. Huang, J. Yang, Y. Zhu, Pulmonary nodule segmentation with CT sample synthesis using adversarial networks, *Med. Phys.* 46 (2019) 1218–1229.
- [143] Y. Chi, L. Bi, J. Kim, D. Feng, A. Kumar, Controlled synthesis of dermoscopic images via a new color labeled generative style transfer network to enhance melanoma segmentation, in: *2018 40th Annu. Int. Conf. IEEE Eng. Med. Biol. Soc.*, IEEE, 2018, pp. 2591–2594.
- [144] Y. Lei, X. Dong, Z. Tian, Y. Liu, S. Tian, T. Wang, X. Jiang, P. Patel, A.B. Jani, H. Mao, CT prostate segmentation based on synthetic MRI-aided deep attention fully convolution network, *Med. Phys.* 47 (2020) 530–540.
- [145] S. Aida, J. Okugawa, S. Fujisaka, T. Kasai, H. Kameda, T. Sugiyama, Deep learning of cancer stem cell morphology using conditional generative adversarial networks, *Biomolecules* 10 (2020) 931.
- [146] T. Goel, R. Murugan, S. Mirjalili, D.K. Chakrabarty, Automatic screening of COVID-19 using an optimized generative adversarial network, *Cognit. Comput.* (2021) 1–16.
- [147] J. Rasheed, A.A. Hameed, C. Djeddi, A. Jamil, F. Al-Turjman, A machine learning-based framework for diagnosis of COVID-19 from chest X-ray images, *Interdiscipl. Sci. Comput. Life Sci.* 13 (2021) 103–117.
- [148] S. Karakanis, G. Leontidis, Lightweight deep learning models for detecting COVID-19 from chest X-ray images, *Comput. Biol. Med.* 130 (2021) 104181.
- [149] Y. Jiang, H. Chen, M.H. Loew, H. Ko, COVID-19 CT image synthesis with a conditional generative adversarial network, *IEEE J. Biomed. Heal. Inf.* (2020).

- [150] M. Loey, G. Manogaran, N.E.M. Khalifa, A deep transfer learning model with classical data augmentation and cgan to detect covid-19 from chest ct radiography digital images, *Neural Comput. Appl.* (2020) 1–13.
- [151] Q. Zhang, Z. Chen, G. Liu, W. Zhang, Q. Du, J. Tan, Q. Gao, Artificial intelligence clinicians can use chest computed tomography technology to automatically diagnose coronavirus disease 2019 (COVID-19) pneumonia and enhance low-quality images, *Infect. Drug Resist.* 14 (2021) 671.
- [152] J. Song, H. Wang, Y. Liu, W. Wu, G. Dai, Z. Wu, P. Zhu, W. Zhang, K.W. Yeom, K. Deng, End-to-end automatic differentiation of the coronavirus disease 2019 (COVID-19) from viral pneumonia based on chest CT, *Eur. J. Nucl. Med. Mol. Imag.* 47 (2020) 2516–2524.
- [153] M.A. Mazurowski, Artificial intelligence may cause a significant disruption to the radiology workforce, *J. Am. Coll. Radiol.* 16 (2019) 1077–1082, <https://doi.org/10.1016/j.jacr.2019.01.026>.
- [154] D.C. Angus, Randomized clinical trials of artificial intelligence, *JAMA, J. Am. Med. Assoc.* 323 (2020) 1043–1045, <https://doi.org/10.1001/jama.2020.1039>.
- [155] Y. Mirsky, T. Mahler, I. Shelef, Y. Elovici, CT-GAN: Malicious tampering of 3D medical imagery using deep learning, *Proc. 28th USENIX Secur. Symp.* (2019) 461–478.